A Case Study of the Interaction of a Mesoscale Gravity Wave with a Mesoscale Convective System

JAMES H. RUPPERT JR.

Department of Atmospheric Science, Colorado State University, Fort Collins, Colorado

LANCE F. BOSART

Department of Atmospheric and Environmental Sciences, University at Albany, State University of New York, Albany, New York

(Manuscript received 25 August 2013, in final form 12 November 2013)

ABSTRACT

This study documents the high-amplitude mesoscale gravity wave (MGW) event of 7 March 2008 in which two MGWs strongly impacted the sensible weather over a large portion of the Southeast United States. These MGWs exhibited starkly contrasting character despite propagating within similar environments. The primary (i.e., long lived) MGW was manifest by a solitary wave of depression associated with rapid sinking motion and adiabatic warming, while the secondary (short lived) MGW was manifest by a solitary wave of elevation ("MGW_{EL}"), dominated by rising motion and moist adiabatic cooling. Genesis of the primary MGW occurred as a strong cold front arrived at the foot of Mexico's high terrain and perturbed the appreciable overriding flow. The resulting gravity wave became ducted in the presence of a low-level frontal stable layer, and caused surface pressure falls up to ~4 hPa. The MGW later amplified as it became coupled with a stratiform precipitation system, which led to its evolution into an intense mesohigh–wake low couplet. This couplet propagated as a ducted MGW attached to a stratiform system for ~12 h thereafter, and induced rapid surface pressure falls of ≥10 hPa (including a fall of 6.7 hPa in 10 min), rapid wind vector changes (e.g., 17 m s^{-1} in 25 min), and high wind gusts (e.g., 20 m s^{-1}) across several states. MGW_{EL} appeared within the remnants of a squall line, and was manifest by a sharp pressure ridge of ~6 hPa with a narrow embedded rainband following the motion of a surface cold front. MGW_{EL} bore resemblance to previously documented gravity waves formed by density currents propagating through stable environments.

1. Introduction

While internal gravity waves are ubiquitous in the atmosphere, those of the scale, amplitude, and duration to substantially impact the sensible weather and become a forecast concern are relatively rare and usually connected to high-amplitude, strongly unbalanced synoptic-scale flow patterns (Uccellini and Koch 1987, hereafter UK87; Plougonven and Zhang 2014). In particular, gravity waves of wavelength ≥50 km and period ≥1 h, which are henceforth referred to as mesoscale gravity waves (MGWs), have been connected with rapid fluctuations in precipitation intensity and distribution, thunderstorm activity, surface pressure, cloudiness, surface winds, and turbulence activity (Brunk 1949; Tepper 1951; Wagner 1962; Ferguson 1967; Bosart and Cussen 1973; Eom 1975; Uccellini 1975; Miller and Sanders 1980; Bosart and Sanders 1986; Bosart and Seimon 1988; Koch et al. 1988; Ralph et al. 1993, hereafter RCV93; Ramamurthy et al. 1993; Bosart et al. 1998; Trexler and Koch 2000). Provided that a wave duct (Lindzen and Tung 1976) is present to permit long MGW duration (~8 h or greater), MGWs can induce banding and sharp breaks in otherwise contiguous cloud and precipitation shields, and can modify and initiate convection in unstable environments (e.g., Brunk 1949; Uccellini 1975; Bosart et al. 1998). Uccellini (1975) reported on a case in which a long-duration MGW train of 2.5-hPa surface pressure amplitude and 300–450-km wavelength both modulated the intensity of preexisting severe thunderstorms and initiated new deep convection

Corresponding author address: James H. Ruppert Jr., Department of Atmospheric Science, Colorado State University, 1371 Campus Delivery, Fort Collins, CO 80523.
E-mail: ruppert@atmos.colostate.edu

DOI: 10.1175/MWR-D-13-00274.1

by enhancing low-level convergence in a convectively unstable air mass. Subsequent studies have provided supporting evidence that MGWs are capable of both modifying and initiating deep convection (Stobie et al. 1983; Pecnick and Young 1984; Bosart and Sanders 1986; Ferretti et al. 1988; Koch et al. 1988; RCV93; Bosart et al. 1998). The manner in which MGWs are *modified by* convection, however, remains largely unclear.

MGWs usually occur within high-amplitude synoptic flow patterns, since typically only these patterns provide the suite of ingredients necessary for MGW genesis, amplification, and maintenance over long periods. The most prolific gravity wave genesis mechanism cited in the MGW literature is geostrophic adjustment (e.g., Blumen 1972; Van Tuyl and Young 1982; UK87). Recent work describes this genesis process (''spontaneous gravity wave emission'') as follows: inertia–gravity waves (synonymous to MGWs in physical character) are continuously emitted in connection with the flow imbalance that develops near the exit regions of upper-level jet streaks during the nonlinear evolution of a baroclinic jet–front system (Zhang 2004; Snyder et al. 2007, 2009; Wang et al. 2009; Wang and Zhang 2010; Plougonven and Zhang 2014).

Surface cold fronts connected to intense jet–front systems can also provide a source of MGW emission. As Ralph et al. (1999) described, a strong cold front can act as an obstacle to the front-relative, cross-front overriding flow, similar to the role of a mountain for topographic waves. When this cross-front flow becomes strong due to rapid frontogenesis (Snyder et al. 1993; Plougonven and Snyder 2007; Lin and Zhang 2008) or terrain influences on frontal motion (Ralph et al. 1999; Neiman et al. 2001), MGWs are excited in response, which can then propagate independent of the cold front if conditions are suitable for wave ducting (Knippertz et al. 2010).

While MGWs at times propagate as wave packets (e.g., Eom 1975; Uccellini 1975; Bosart and Sanders 1986), they can also be characterized by solitary pressure waves of elevation or depression (e.g., Bosart and Cussen 1973; Christie et al. 1979; Pecnick and Young 1984; Lin and Goff 1988; Ramamurthy et al. 1993). Such solitary pressure waves (denoted solitons) are thought to arise from a balance between inertial advection, a nonlinear process that steepens the wave, and wave dispersion, which causes all but the largest-wavelength wave to be dispersed (Christie et al. 1979; Lin and Goff 1988; Lin 2010).

A primary ingredient for long-duration MGWs is a wave duct, which, according to linear theory (Lindzen and Tung 1976), is composed of a low-level stable layer overlain by a layer of negligible stability (i.e., a reflecting layer) in which the flow at some level matches MGW phase speed and direction (i.e., a critical level). This wave duct prevents the vertical propagation of gravity wave energy, thereby keeping it in the troposphere. Although the environment is not often capable of perfectly ducting wave energy, vertical wind shear and/or diabatic heating can provide a compensating energy source to maintain the MGW (e.g., Lalas and Einaudi 1976; Stobie et al. 1983; Pecnick and Young 1984; UK87). Such was the case with the well-documented MGW associated with surface pressure falls exceeding 13 hPa $(30\,\text{min})^{-1}$ and strong fluctuations in snowfall rates along the Atlantic seaboard on 4 January 1994 (Bosart et al. 1998). Zhang et al. (2001) demonstrated that the strongly vertically sheared flow in that case provided a steady energy source to the incipient MGW as it propagated within an imperfect wave duct. The MGW rapidly amplified, however, upon initiating a band of elevated convection, to which it then became coupled via the wave–conditional instability of the second kind (CISK) mechanism (Lindzen 1974; Raymond 1984). This coupling led to a dramatic increase of the extraction of wave energy from the flow, which was argued to be the cause for sudden MGW amplification (Zhang et al. 2001).

While previous studies have provided insights as to how convection is *modified by* MGWs, studies documenting the processes through which convection *modifies* MGWs are limited owing to the lack of relevant observations and the complexity of processes involved. The present study attempts to fill this gap by describing the 7 March 2008 MGW event in which rapid MGW amplification was clearly connected with mesoscale organized convection. This MGW lasted over 16 h, impacting the sensible weather over much of the southern and southeastern United States. Since the MGW and associated precipitation signatures were well sampled by the operational radar network and a high-frequency basic observation network, this case offers an unprecedented opportunity to document the complex role of diabatic processes in the MGW life cycle.

2. Data and methodology

The 7 March 2008 MGW case was documented using the 5-min ASOS dataset [Automated Surface Observing System (ASOS); Nadolski 1998] from the National Oceanic and Atmospheric Administration (NOAA) National Climatic Data Center (NCDC; http://www.ncdc.noaa.gov/), the Rawinsonde Observation dataset from the University of Wyoming upper-air repository (http://weather.uwyo.edu/upperair/), the National cloud-to-ground (CG) lightning dataset from the National Lightning Detection Network (http://www.unidata.ucar.edu/data/lightning/nldn.html), the Level II Weather Surveillance Radar–1988 Doppler (WSR-88D) dataset

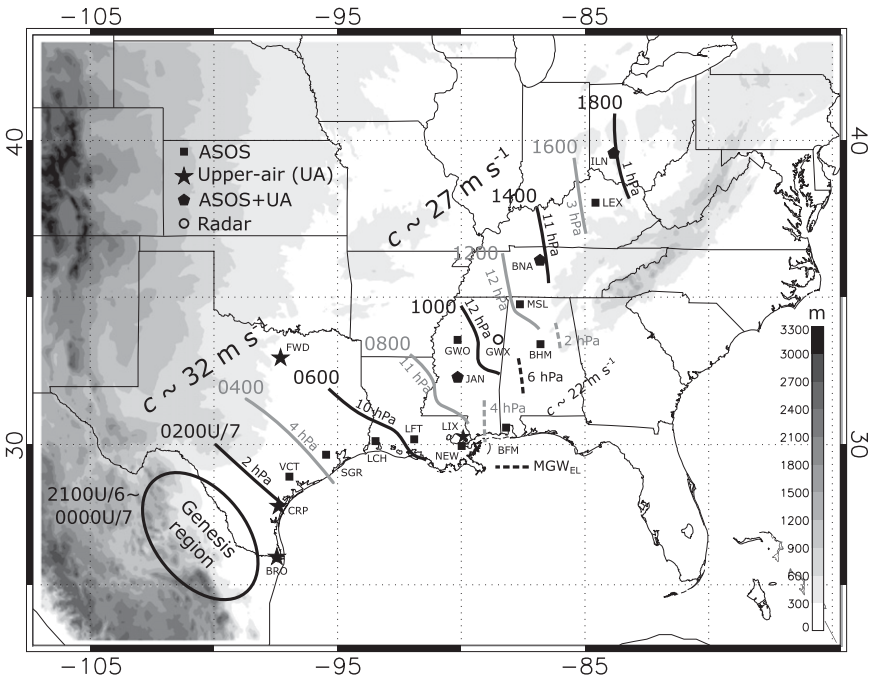

FIG. 1. Isochrone analysis of the mesoscale gravity waves (MGWs) of 7 Mar 2008. Time/date is indicated according to the format 0000U/7 (for 0000 UTC 7 Mar). The ellipse indicates the genesis region of the primary MGW, a wave of depression, and the solid lines denote the associated positions of minimum surface pressure. The dashed lines denote the position of a wave of elevation (MGW_{EL}) connected to a surface cold front. Ground-relative phase speed c is indicated for both the primary MGW (at two different stages) and the MGW_{EL}. Maximum surface pressure changes are provided with each isochrone. Stations are indicated for reference. Topography is shaded according to the color bar (m).

from NCDC, and the Geostationary Operational Environmental Satellite dataset from the Man computer Interactive Data Access System (http://www.ssec.wisc.edu/mcidas/).

ASOS data provides the suite of basic surface variables, the most important of which is pressure (derived from altimeter settings) and wind. The radar data were analyzed with the aid of routines provided by the Radar Software Library under National Aeronautics and Space Administration Tropical Rainfall Measuring Mission Office (http://trmm-fc.gsfc.nasa.gov/trmm_gv/software/rsl/). The Gibson Ridge GR2Analyst software package was employed to generate vertical radar cross sections (Figs. 11 and 15; http://www.grlevelx.com/gr2analyst/).

Supplementing the above observational datasets are two operational model datasets from the National Centers for Environmental Prediction (NCEP): 1) the half-degree Global Forecast System (GFS), and 2) the 13-km Rapid Update Cycle (RUC). These model analyses were collected from the NOAA National Operational Model Archive and Distribution System (http://nomads.ncdc.noaa.gov/). While substantial insights can be gained about MGW vertical structure from profiler data (RCV93; Bosart et al. 1998; Trexler and Koch 2000), data dropouts in the NOAA Profiler Network at the relevant sites rendered this product inadequate for the present study.

3. Overview of 7 March 2008

Two MGWs were observed on 7 March 2008 (Fig. 1). The primary MGW was a long-lived, high-amplitude wave of depression associated with a rapid surface pressure fall, which was often preceded or followed by a smaller increase in pressure. A secondary, more short-lived MGW was characterized by a wave of elevation, which will be denoted MGW_{EL} to distinguish it from the wave of depression.

The primary MGW was akin to solitary waves of depression that have been documented by previous studies (e.g., Brunk 1949; Ferguson 1967; Pecnick and Young 1984; Lin and Goff 1988; Bosart et al. 1998). It first appeared in the ASOS network near the Texas–Mexico border around 0200 UTC 7 March [Fig. 1; unless specified, all UTC times are for 7 March; subtract 6 h for

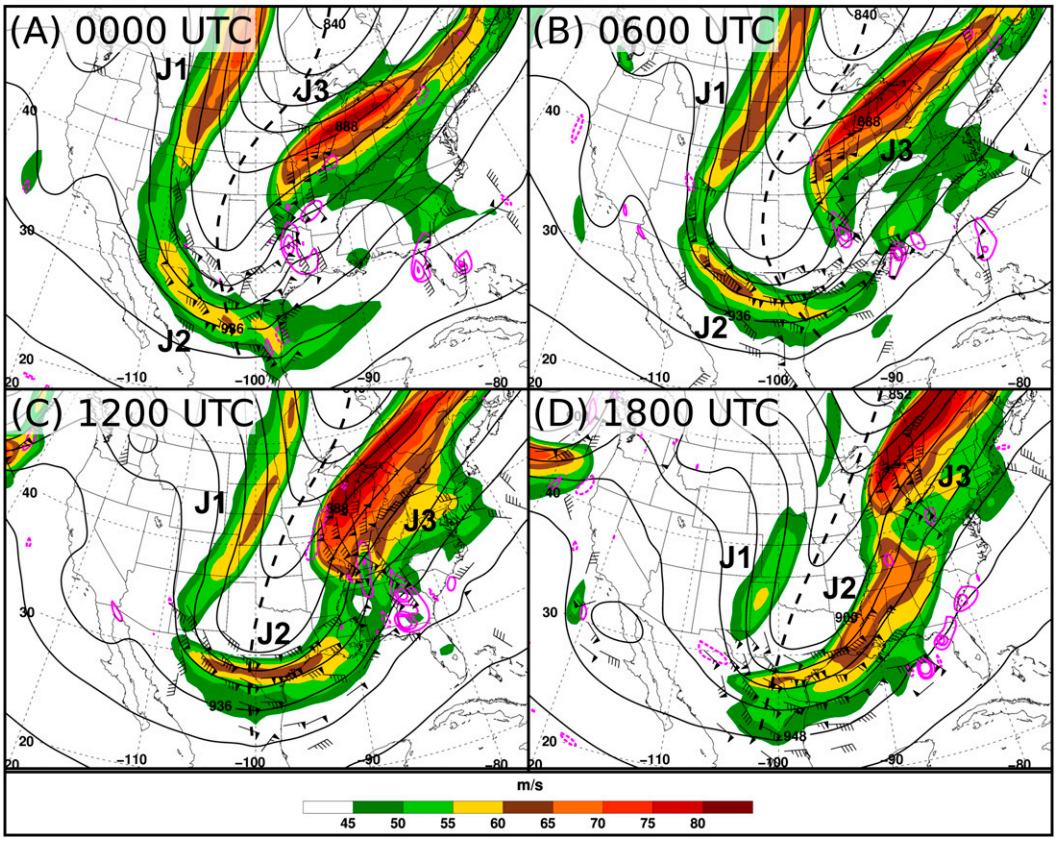

FIG. 2. Maps of 300-hPa geopotential height (black contours; every 12 dam), total wind speed (shaded according to the color bar; $m\,s^{-1}$), ageostrophic flow (wind barbs; pennants, full barbs, and half barbs correspond to 25, 5, and 2.5 $m\,s^{-1}$, respectively), and divergence (magenta contours; ± 8, 16, and $24 \times 10^{-5}\,s^{-1}$; dashed for negative values) at (a) 0000, (b) 0600, (c) 1200, and (d) 1800 UTC 7 Mar. Black dashed lines denote trough axes (maps of potential vorticity on the dynamic tropopause were consulted for placement of trough axes; not shown). J1, J2, and J3 denote three jet streaks referred to in the text. Fields are from operational half-degree Global Forecast System (GFS) analyses.

local time (CST)]. Evidence suggests that its genesis occurred in northeastern Mexico several hours prior (section 6a). The MGW was initially characterized by a northeastward-propagating solitary ~2-hPa pressure fall with ground-relative phase speed c, ~32 $m\,s^{-1}$, with an absence of precipitation (section 4a). The maximum crest-to-trough pressure fall in the MGW rapidly increased to ~10 hPa around 0600 UTC along its southeastward section as the MGW slowed ($c \sim 27\,m\,s^{-1}$) and interacted with a mature MCS (section 4b). The associated pressure fall persisted at ≥10 hPa from 0600 to 1400 UTC, during which period it remained tied to the back edge of an extensive stratiform rain shield (section 4c). The MGW rapidly lost amplitude after 1400 UTC, and was difficult to identify in ASOS and radar data beyond 1800 UTC (section 4d).

MGW_{EL} was characterized by a sharp, solitary wave of elevation that appeared along the coast of the Gulf of Mexico around 0600 UTC, which was associated with rapid surface pressure changes of up to 6 hPa (1100 UTC) and often attended by a narrow rainband (Fig. 1; section 5). MGW_{EL} remained connected to a cold front as it progressed northeastward, and resembled similar previously documented MGWs formed by density currents propagating through a stable air mass (e.g., Christie et al. 1979; Ramamurthy et al. 1993; Koch et al. 2008).

The emphasis of this study is placed on the wave of depression because it exerted strong impacts on the sensible weather over a large region of the Southeast United States. The wave of elevation was relatively short lived (Fig. 1), had less of an impact on sensible weather, and hence will be discussed in less detail. The notation "MGW" in subsequent text refers to the primary wave of depression, while the notation "MGW_{EL}" is employed for the wave of elevation (Fig. 1). An analysis of MGW_{EL} is provided in section 5.

Synoptic analysis

Upper-level flow maps depicting the synoptic evolution on 7 March are provided in Fig. 2. A deep 300-hPa

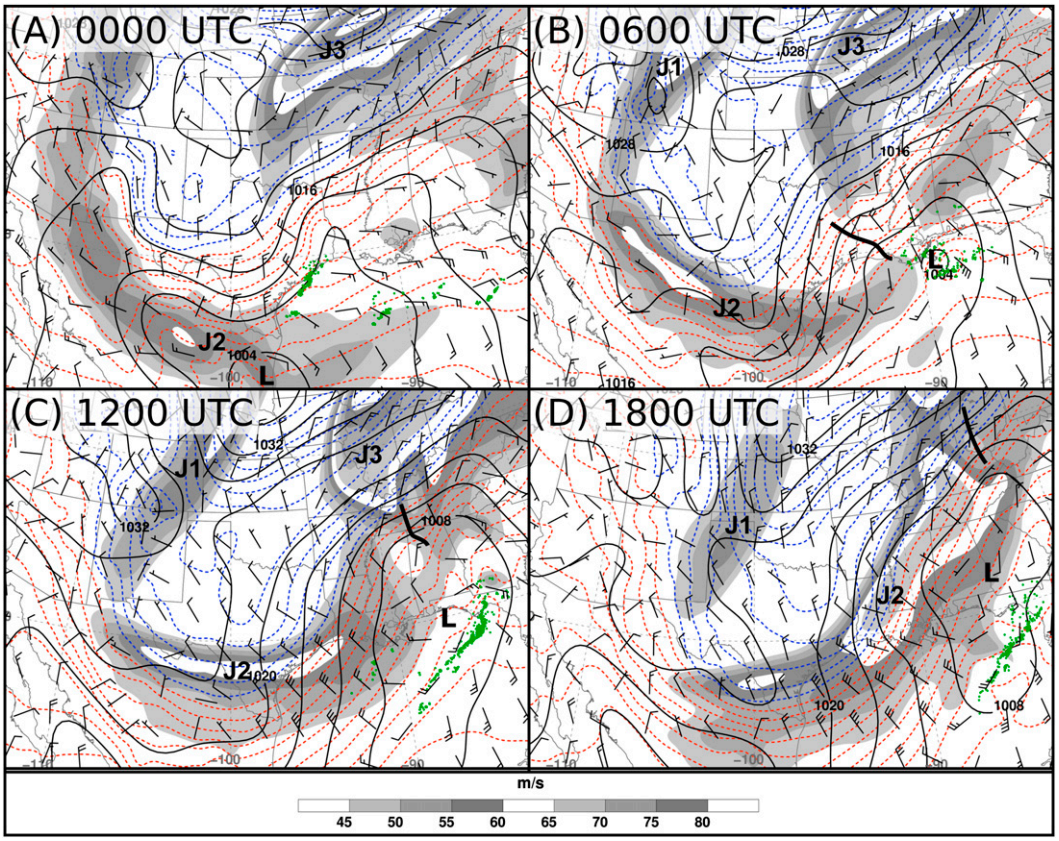

FIG. 3. Maps of mean sea level pressure (SLP; black contours; every 4 hPa), 10-m wind (barbs; format is as in Fig. 2), 1000–500-hPa thickness (dashed contours; every 3 dam; blue for thickness ≤540 dam), and cloud-to-ground (CG) lightning strike locations within the preceding 5 min (green dots) at (a) 0000, (b) 0600, (c) 1200, and (d) 1800 UTC 7 Mar. 300-hPa wind speed (shaded according to the color bar; $m\,s^{-1}$) is repeated here from Fig. 2 to demonstrate connections between upper- and lower-level features. Thick black lines denote positions of the primary MGW (Fig. 1). Model fields are from GFS analyses.

trough is situated over the central United States, marked by jet streaks situated upstream (''J1''), within (''J2''), and downstream (''J3'') of the trough base (Figs. 2a–d). The trough exhibits negative tilt along its southern extent from 0000–1200 UTC, and becomes positively tilted by 1800 UTC. The trough base is characterized by upstream-directed ageostrophic flow, $\mathbf{v}_a \sim 50\,m\,s^{-1}$, consistent with cyclonic flow curvature, with a region of $>25\,m\,s^{-1}$ down-height-gradient $\mathbf{v}_a$ in the entrance region of J3. This region of downgradient $\mathbf{v}_a$ increases in area from 0600 to 1200 UTC as J3 widens (e.g., over Illinois) in connection with widespread stratiform precipitation (shown below). Divergence exceeding $24 \times 10^{-5}\,s^{-1}$ appears in the region of diffluent $\mathbf{v}_a$ near the inflection point over eastern Texas (TX) at 0000 UTC. This region of divergence shifts from eastern TX into Tennessee (TN), Kentucky (KY), and Georgia (GA) from 0000 to 1200 UTC, after which time J2 and J3 begin to merge, the trough loses its negative tilt, and the region of diffluent $\mathbf{v}_a$ and divergence all but disappears.

The 6-hourly maps of mean sea level pressure (SLP) are provided in Fig. 3. A cyclone is initially positioned on the leeside of the Sierra Madre Oriental mountain range (SMO; Fig. 1) in northeastern Mexico beneath the exit region of J2 (Fig. 3a). Consistent with thermal wind balance, the jet streaks are largely collocated with a pronounced baroclinic zone, which is draped from the TX–Mexico border northeastward. There is cold air advection (CAA) across TX and northern Mexico beneath the trough base, indicative of trough deepening. The cold front is attended by deep convection along the TX coast, as indicated by CG lightning flashes. By 0600 UTC, the cold front stretches into the Gulf of Mexico (GoM) and the low and deep convection are situated near the central GoM coast and a region of 300-hPa divergence (Figs. 2b and 3b). The MGW is situated in a northwest–southeast-oriented inverted trough west of the surface cyclone, which is much weaker than in observations (Fig. 8, later). As the surface cyclone and deep convection shift eastward from 0600 to 1800 UTC, the

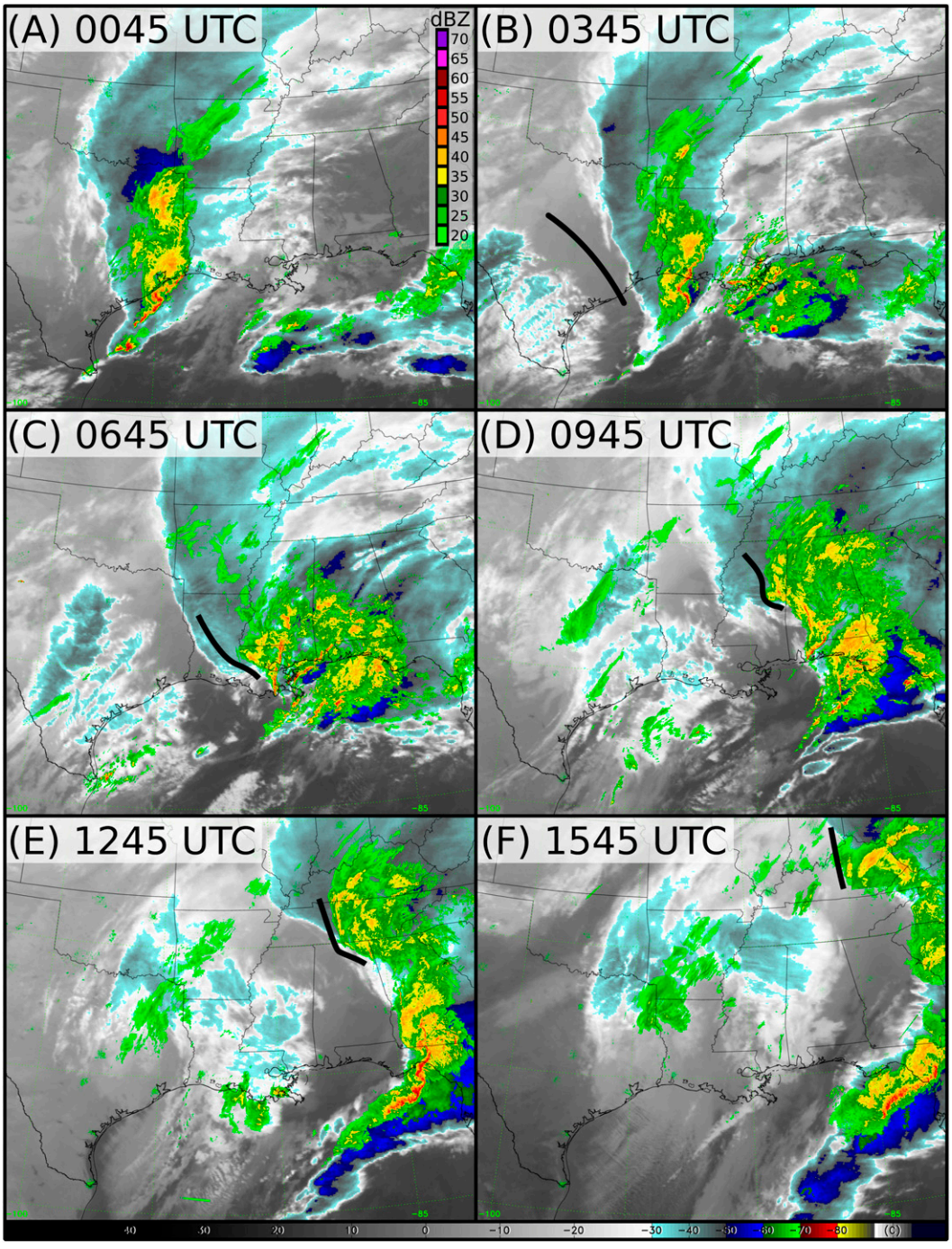

FIG. 4. Infrared satellite brightness temperature (shaded according to the color bar at bottom; °C) with mosaic WSR-88D base reflectivity overlaid [shaded according to the color bar in (a)] at (a) 0045, (b) 0345, (c) 0645, (d) 0945, (e) 1245, and (f) 1545 UTC 7 Mar. Thick black lines denote positions of the primary MGW (Fig. 1).

MGW propagates northeastward, remaining on the cold side of the cold front and near the area of implied ascent based on the 300-hPa flow pattern (Figs. 3b–d).

The 3-hourly maps of infrared satellite brightness temperature overlaid by mosaic base radar reflectivity are provided over the Southeast United States for 0045–1545 UTC (Fig. 4). All base reflectivity data in the depicted region were collected for a given time. Data were then plotted for the locations nearest to their parent station, yielding a base reflectivity mosaic of the

lowest-elevation data possible. A southwest–northeast-oriented squall line is situated along the cold front at 0045 UTC, with a lightning-free adjoining stratiform region to the north (Figs. 3a and 4a). Cold clouds (<-30°C) and the stratiform region extend far northward of the deep convection, consistent with hydrometeor advection in strong southerly sheared flow (Parker and Johnson 2000). By 0345 UTC, the MCS has shifted eastward, a trailing stratiform precipitation region has developed, and the cold-cloud shield has developed a sharper trailing edge (Fig. 4b). The MGW is situated in a region markedly devoid of clouds trailing the MCS, consistent with enhanced subsidence. By 0645 UTC, stratiform precipitation has developed over much of southern Mississippi (MS) and Alabama (AL) and offshore (which is mostly lightning free), consistent with increased forcing for ascent and southwesterly vertical shear as J3 approaches from the southwest (Figs. 2b, 3b, and 4c). The MGW is closely aligned with the trailing edge of the cold-cloud shield and stratiform rain shield, a connection that persists through 1545 UTC, with enhanced rainfall appearing ahead of the MGW at times (Figs. 4c–f). The stratiform rain shield substantially decreases in size by 1545 UTC (Fig. 4f). The MGW–cloud and rainfall relationships shown here are consistent with previous studies (e.g., Eom 1975; Bosart and Sanders 1986; Bosart and Seimon 1988; Lin and Goff 1988; RCV93; Bosart et al. 1998).

Figures 1–4 demonstrate that the MGW exhibited its greatest amplification as it became collocated with the back edge of a MCS stratiform precipitation region (~0600 UTC), which occurred on the cold side of a cold front. Subsequent to this MGW amplification, the stratiform precipitation shield expanded and shifted northeastward as the width of the J3 entrance region and the associated area of down-height-gradient $\mathbf{v}_a$ expanded (Figs. 2b,c). This 300-hPa flow evolution is consistent with the maintenance of an upper-level divergent outflow associated with enhanced stratiform precipitation. Throughout this progression, the MGW remained attached to the trailing edge of the stratiform precipitation shield.

4. Mesoanalysis of the MGW life cycle

a. Genesis

Figure 5 provides meteograms generated from 5-min ASOS data for selected stations along the track of the MGW (Fig. 1). The meteograms include perturbation pressure with the 10-h mean removed, p', and flow component in the direction of MGW propagation with the 10-h mean removed, u'. Meteograms from Victoria (VCT; Fig. 5a) and Sugarland (SGR; Fig. 5b), TX, illustrate characteristics of the MGW around genesis. MGW passage at VCT is indicated by a brief (~2 h) negative p' perturbation ($\Delta p' \sim 2$–3 hPa) embedded within a synoptic-scale pressure rise (Figs. 3a,b), increased gustiness, and temporary strengthening and veering of the wind to northerly. The p' evolution suggests a wave period, $T \sim 2.25$ h. The vector wind change is reflected in a reduction in u' ($\Delta u' \sim 4\,\mathrm{m\,s^{-1}}$), closely matching the pattern in p'. MGW passage at SGR, farther northeast, occurs after 0400 UTC and exhibits similar characteristics to that at VCT, except for larger $\Delta p'$ (~4 hPa). There is a subtle dual-minimum structure in p' at VCT and SGR.

Such close correlation between surface p' and u', as seen in Fig. 5, is a fundamental characteristic of ducted MGWs owing to the polarization relation of internal gravity waves that are largely in hydrostatic balance (Eom 1975; Bosart and Sanders 1986; RCV93). This relation implies that surface divergence is shifted out of phase with p', such that sinking (rising) motion and adiabatic warming (cooling) lead (trail) the p' minimum by a quarter wavelength, resulting in the gravity wave's propagation.

A surface mesoanalysis is provided for 0300 UTC in Fig. 6. The pressure analysis was derived from time–space conversion of 5-min ASOS time series (e.g., Fig. 5; Fujita 1955). A bowing squall line with trailing stratiform precipitation in the colder air marks the arrival of the frontal zone in southwestern Louisiana (LA) and the northern GoM around 0300 UTC (Figs. 3a, 4a,b, and 6). The enhanced pressure gradient and baroclinic zone within the MCS suggest early formation of a mesohigh in response to cooling from evaporation and melting (Fig. 6; Fujita 1959). A locally enhanced temperature gradient also exists along the TX–Mexico border where the northwest–southeast-oriented isotherms reflect cold-air damming against the SMO (Fig. 1).

The MGW is manifest by a sharp northwest–southeast-aligned inverted trough over Texas, which is led by a broader and weaker inverted ridge (Fig. 6). Its horizontal wavelength λ is ~300 km. Taking $c = \lambda/T$, with $T \sim 2.25$ h (Figs. 5a,b), yields a value of $c \sim 37\,\mathrm{m\,s^{-1}}$, which is in reasonable agreement with the estimate of $32\,\mathrm{m\,s^{-1}}$ from isochrone spacing (Fig. 1). As this MGW trough–ridge couplet propagates northeastward across TX, a slow increase in SLP occurs as the MGW ridge approaches a given location (subtracting the synoptic tendency), and is followed by a sharper, larger SLP fall as the trough passes (Figs. 5a,b and 6). Also depicted in Fig. 6 is enhanced (reduced) flow in the direction opposing MGW propagation within the trough (ridge), consistent with the ducted gravity wave model (RCV93) and the u' and total wind time series in Figs. 5a,b.

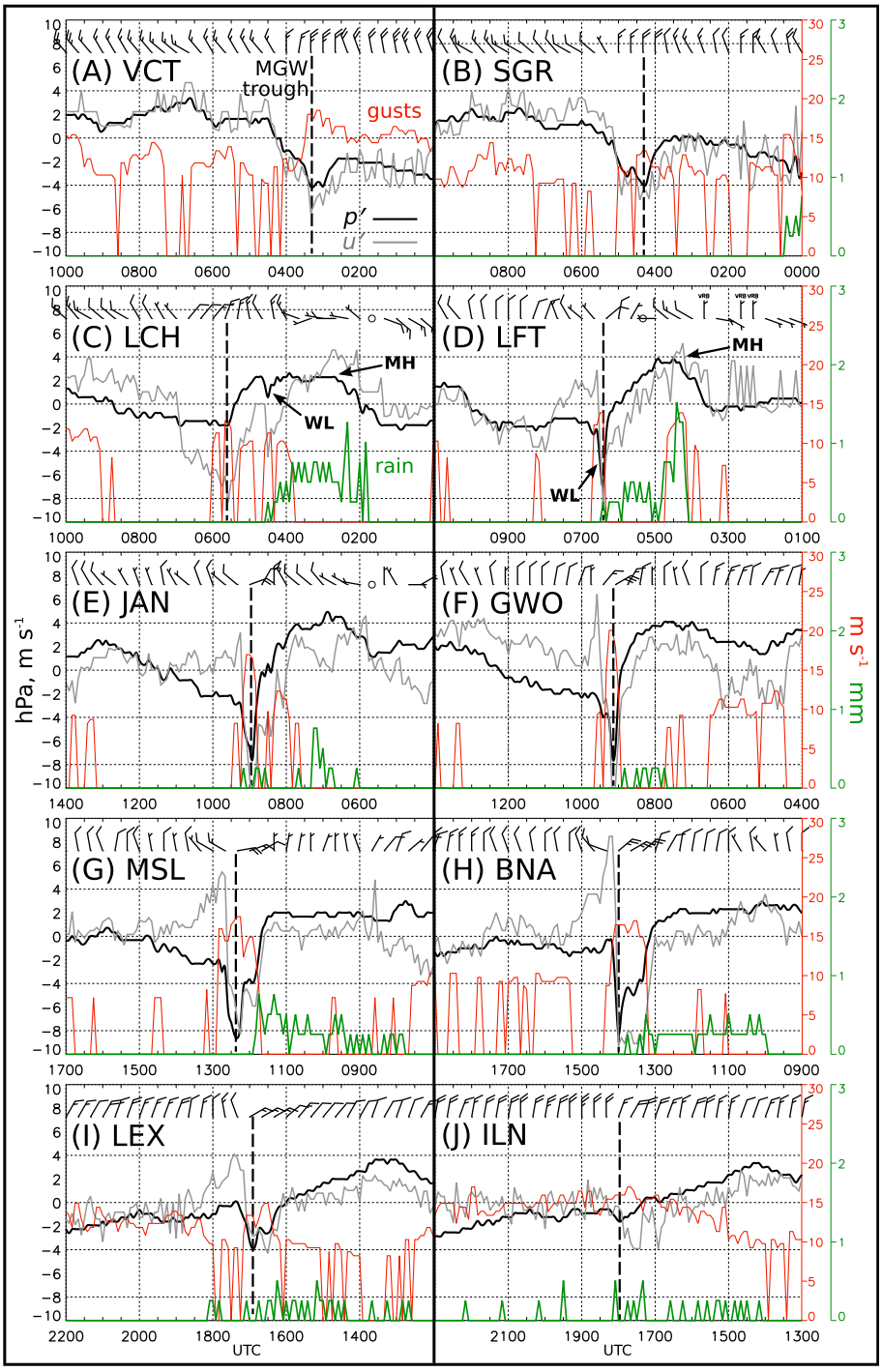

FIG. 5. Meteograms for the primary MGW from five-minute ASOS data on 7 Mar 2008 (time increases toward the left), with 10-m wind (barbs in format of Fig. 2), perturbation pressure with 10-h mean removed, p' (black line; hPa; black ordinate scale), flow component in the direction of wave propagation with 10-h mean removed, u' (gray line; m s^{-1}; black ordinate scale), 5-min accumulated rainfall (green line; mm; green ordinate scale), and wind gusts (red line; m s^{-1}; red ordinate scale). The vertical dashed lines indicate MGW trough passage. "WL" ("MH") indicates the feature resembling a developing wake low (mesohigh), as discussed in the text. (a) Victoria (VCT) and (b) Sugar Land (SGR), Texas (TX); (c) Lake Charles (LCH) and (d) Lafayette (LFT), Louisiana; (e) Jackson (JAN) and (f) Greenwood (GWO), Mississippi (MS); (g) Muscle Shoals (MSL), Alabama (AL); (h) Nashville (BNA), Tennessee (TN); (i) Lexington (LEX), Kentucky; and (j) Wilmington (ILN), Ohio (OH). See Fig. 1 for station locations.

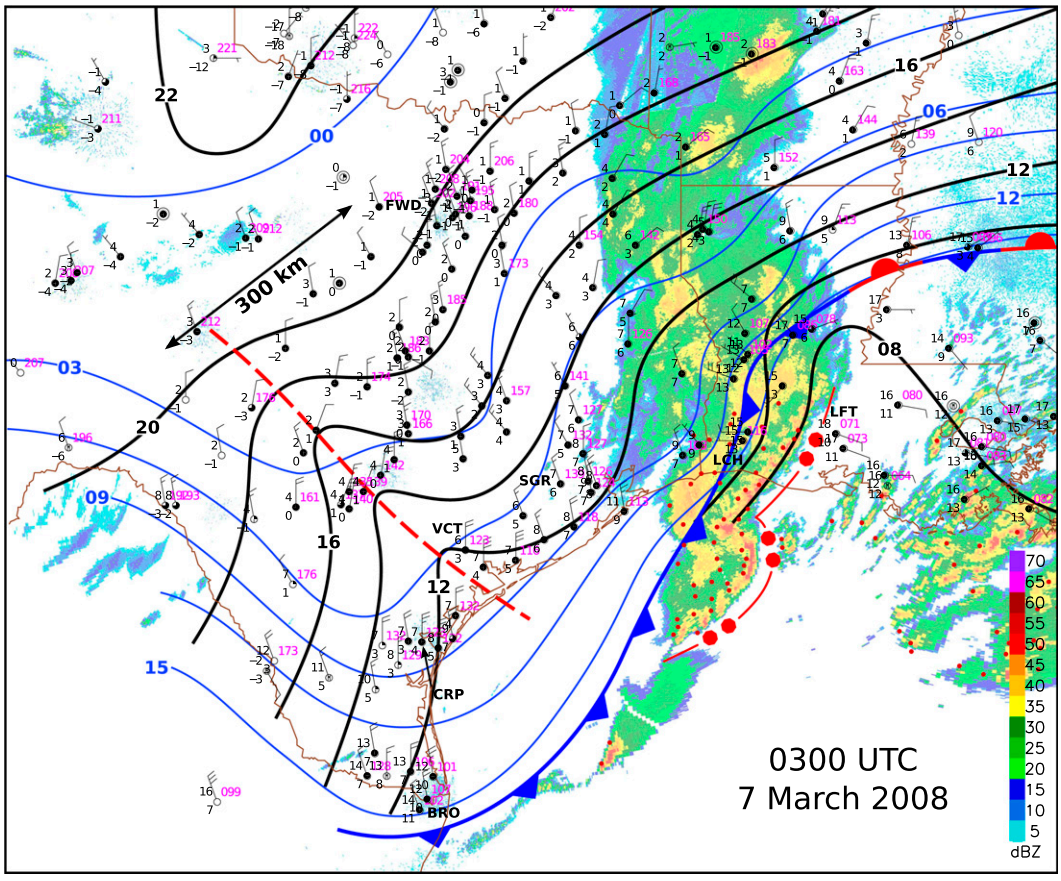

FIG. 6. Manual surface analysis for 0300 UTC 7 Mar including mosaic base reflectivity (dBZ; according to the color bar), SLP contoured in black (every 2 hPa; first two digits left off), and temperature contoured in blue (every 2°C). Fronts and squall lines are plotted in standard convention. Red dashed line denotes the MGW trough axis. The length scale indicates the approximate MGW horizontal wavelength λ. Surface station data are plotted in standard convention, including sky cover, temperature and dewpoint temperature (°C), SLP, and wind (format is as in Fig. 2). Small red dots indicate 5-min CG lightning strikes, which have been thinned for clarity. Key stations are indicated by their three-letter identifiers (Fig. 1).

Skew T–log$p$ diagrams are provided from selected sounding stations along the track of the MGW (Fig. 7), which include intrinsic phase speed, $C^* = c - U$ (where U is the flow component in the direction of MGW propagation, ~55°), and Richardson number Ri defined here as

$$\mathrm{Ri} = \frac{g}{\theta}\frac{\partial\theta}{\partial z}\Big/\left(\frac{\partial U}{\partial z}\right)^2, \qquad (1)$$

where g is gravity and θ is potential temperature. Comparison of the Corpus Christi (CRP) and Brownsville (BRO), TX, soundings for 0000 UTC (Fig. 7a) indicates that the cold front—situated between the two stations (Fig. 3a)—separates a cool, moist, and stable postfrontal low-level air mass (CRP) from a convectively unstable prefrontal air mass (BRO). The postfrontal air is capped by a dry air mass with a steep lapse rate of likely Mexican origin, while the unstable prefrontal air, likely of GoM origin, is weakly capped. At CRP, a critical level (where $C^* = 0$) is found near 375 hPa, just above the layer of steepest lapse rates. According to Lindzen and Tung (1976), a critical level must be situated within the layer of reduced stability above the low-level layer of higher stability in order for wave energy to be ducted. This would suggest that conditions are inadequate for ducting at CRP at this time; however, RUC analyses (shown later; section 6a) suggest that the critical level shifts downward into the steeper-lapse-rate air as the upper-level trough and J1 advance northeastward (Figs. 2a,b).

According to Lindzen and Tung (1976), the intrinsic ducted phase speed supported by a wave duct for the zeroth-order gravity wave mode is

$$C_d^* = \frac{2}{\pi}\left[\frac{gD\Delta\theta}{\bar{\theta}}\right]^{1/2}, \qquad (2)$$

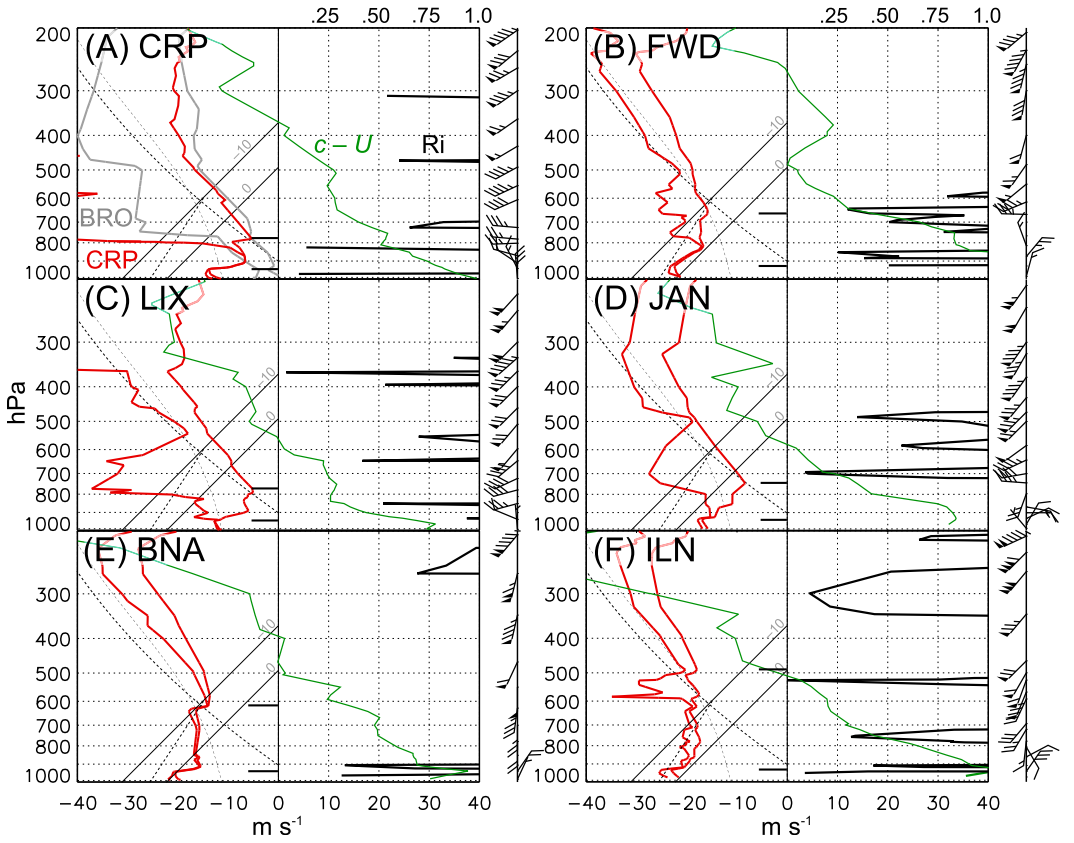

FIG. 7. Sounding profiles from (a) Corpus Christi (CRP) and (b) Fort Worth (FWD), TX; (c) Slidell (LIX), LA; (d) Jackson (JAN), MS; (e) Nashville (BNA), TN; and (f) Wilmington (ILN), OH (see Fig. 1 for station locations). Panels (a) and (b) are from 0000 UTC 7 Mar soundings, and the rest are from 1200 UTC 7 Mar soundings. Panel (a) includes the 0000 UTC 7 Mar Brownsville (BRO), TX, profiles in gray. Plotted are temperature (°C) T and dewpoint temperature (°C) T_d in skew T–log$p$ format (red; −10° and 0°C isotherms are labeled, and one dry adiabat, moist adiabat, and mixing ratio line are included in each), wind (barbs; format is as in Fig. 2), Richardson number Ri (black; top abscissa scale), and MGW intrinsic phase speed, $C^* = c - U$ (see Table 1 for values of c; green; m s^{-1}; bottom abscissa scale) where U is the flow component in the direction of MGW propagation (calculated assuming propagation direction of 55°). Black dashes in the skew T–log$p$ plots indicate the stable ducting layer base (p_{base}) and top (p_{top}) used for calculations in Table 1.

where D is the depth of the stable ducting layer, $\Delta\theta$ is the vertical θ change within this layer, and the overbar denotes the stable-layer mean. The depth D must be deep enough to contain one-quarter of the vertical MGW wavelength, that is, $D \geq D_{\text{crit}}$, where D_{crit} is defined as

$$D_{\text{crit}} = \frac{\pi}{2}\frac{\overline{C^*}}{\overline{N}}, \tag{3}$$

where N is the Brunt–Väisälä frequency (Lindzen and Tung 1976). Equations (2) and (3) are evaluated using parameters obtained from the six soundings shown in Fig. 7 (Table 1). Stable layer base and top (p_{base} and p_{top}, respectively) were selected such that all prominent inversion layers within the column were included. Both p_{base} and p_{top} are shown in Fig. 7 and Table 1. While the effects of moisture could be included through calculation of N for accuracy (Durran and Klemp 1982), the nature of wave ducting is determined more by the wind profile and dry stratification than the variability of moisture. Therefore, (2) and (3), which come from Lindzen and Tung (1976), are suitable for our purposes.

For CRP, D (C_d^*) is about 74% (79%) of D_{crit} ($\overline{C^*}$), indicating that the stable layer at CRP (Fig. 7a) is slightly too shallow to contain the observed MGW by this metric (Table 1); however, the expected evolution following 0000 UTC likely trends toward satisfying the above criteria. Deepening of the cold air likely increases D at CRP as CAA persists; for example, D at Fort Worth (FWD; Fig. 7b), TX, situated deeper within the cold air to the north, is 60% larger than

TABLE 1. Wave duct parameters calculated from the soundings shown in Fig. 7. Sounding station code and time are listed in the first column, followed by pressure at the base (p_{base}) and top (p_{top}) of the stable ducting layer, critical stable ducting layer depth (D_{crit}), observed depth (D), intrinsic ducted phase speed (C_d^*), observed duct-mean intrinsic phase speed ($\overline{C^*}$), ground-relative MGW phase speed (c; Fig. 1), duct-mean θ ($\overline{\theta}$), vertical θ change within the duct ($\Delta\theta$), and duct-mean Brunt–Väisälä frequency ($\overline{N}$). Both p_{base} and p_{top} are plotted in Fig. 7.

	p_{base}, p_{top} (hPa)	D_{crit} (km)	D (km)	C_d^* (m s^{-1})	$\overline{C^*}$ (m s^{-1})	c (m s^{-1})	$\overline{\theta}$ (K)	$\Delta\theta$ (K)	$\overline{N}$ (10^{-2} s^{-1})
CRP 0000 UTC 7 Mar	948, 776	2.27	1.67	20.9	26.3	32.0	296.2	19.5	1.81
FWD 0000 UTC 7 Mar	929, 662	3.30	2.68	29.2	35.6	32.0	288.0	23.1	1.69
LIX 1200 UTC 7 Mar	948, 771	1.30	1.72	20.9	15.2	29.5	297.0	18.9	1.84
JAN 1200 UTC 7 Mar	943, 743	1.83	1.95	23.8	25.4	27.0	292.5	21.4	2.18
BNA 1200 UTC 7 Mar	942, 616	2.29	3.63	35.4	23.2	27.0	291.5	27.3	1.59
ILN 1200 UTC 7 Mar	933, 489	2.29	4.99	49.3	22.3	27.0	288.6	35.4	1.53

that at CRP (Table 1). Larger D leads to larger C_d^* through (2).

At FWD (Fig. 7b), D (C_d^*) is about 81% (82%) of D_{crit} ($\overline{C^*}$), while at Slidell (LIX; Fig. 7c), LA, D (C_d^*) is about 132% (138%) of D_{crit} ($\overline{C^*}$) (Table 1). These calculations indicate that conditions for wave ducting are marginal within the deep, colder air near FWD, where the critical level remains above 400 hPa and there is an absence of steep lapse rates aloft (Fig. 7b). Conditions improve northeastward toward LIX by 1200 UTC, however, where the low-level stable layer is deep and the critical level lies within the midtropospheric layer of steep lapse rates in connection with stronger upper-level flow (Figs. 2a–c and 7c).

b. Amplification and coupling with rainfall

Lake Charles (LCH), LA, experiences squall-line passage around 0145 UTC, as evidenced by a wind shift from southeasterly to westerly and several bursts of convective rainfall [$\sim$1 mm (5 min)$^{-1}$ or 1.2 cm h^{-1}; Figs. 5c and 6]. A $\sim$2-h period of lighter stratiform rainfall follows after a brief reduction in rainfall behind the squall line and wind shift (Figs. 5c and 6). Following the squall-line passage, p' increases by $\sim$4 hPa over an hour with a coinciding increase in u' of $\sim$4 m s^{-1}. This pressure–wind relationship, along with the pattern in rainfall, is consistent with a squall-line mesohigh (MH; Johnson and Hamilton 1988; Johnson 2001). Nearly constant p' is observed during the stratiform rainfall period. Around 0430 UTC, p' and u' briefly decrease ($\Delta p' \sim 2$ hPa and $\Delta u' \sim 4$ m s^{-1}) as rainfall ends and gustiness temporarily increases. This pattern is indicative of the passage of a wake low (WL; e.g., Johnson and Hamilton 1988). This occurs just after a marked increase in northwesterly flow indicating frontal passage (Figs. 5c and 6), which heralds the arrival of a more stable low-level air mass (Fig. 7a). A $\sim$4-hPa decrease in p' occurs shortly following WL passage over a $\sim$45-min period beginning at 0500 UTC, without a subsequent p' recovery. This p' fall occurs in conjunction with surface winds that strengthen and veer from northwesterly to northeasterly, a directional change consistent with surface divergence. Divergence can also be inferred from the negative tendency in u'.

The 0600 UTC mesoanalysis depicts an inverted trough–ridge couplet in SLP overlapping the MCS that is at least 4 hPa higher in amplitude than the MGW couplet depicted at 0300 UTC (Figs. 6 and 8). Furthermore, a very sharp 4-hPa SLP minimum resembling a WL now appears at the back edge of the MCS stratiform region within the broader trough. A cold tongue has formed within the stratiform region and inverted ridge, suggesting the likely role of low-level diabatic cooling in mesohigh formation (Fujita 1959). Locally enhanced CAA behind the cold front, which is now collocated with the squall line, could also be a contributing factor to the cold tongue.

The sharp SLP minimum and inverted ridge within the MCS stratiform region compose a local SLP couplet with a wavelength of $\sim$185–200 km. The pressure, wind, and rainfall relationships within this couplet qualitatively match those in the LCH time series (Fig. 5c), and also match those of a MH–WL couplet (Johnson and Hamilton 1988; Johnson 2001). The span of the broader encompassing trough–ridge couplet over an area greater than the MCS rainfall signatures (e.g., into eastern TX), however, indicates that this broader couplet cannot be attributed to local diabatic processes within the MCS. This broader SLP couplet is indeed part of the MGW that propagated from southern TX (Fig. 6). The MGW wavelength clearly exhibits spatial variation, with a marked increase in wavelength toward the north-northwest away from the squall line (Fig. 8).

The Lafayette (LFT; Fig. 5d), LA, meteogram depicts passage of the MCS and sharp SLP couplet as an initial p' rise of 4 hPa following gust front passage (i.e., the MH), a fall of 5 hPa over $\sim$1.5 h after the MH, a very rapid fall of $\sim$5 hPa, and finally a similarly rapid $\sim$5-hPa recovery. The total magnitude p' fall of $\sim$10 hPa

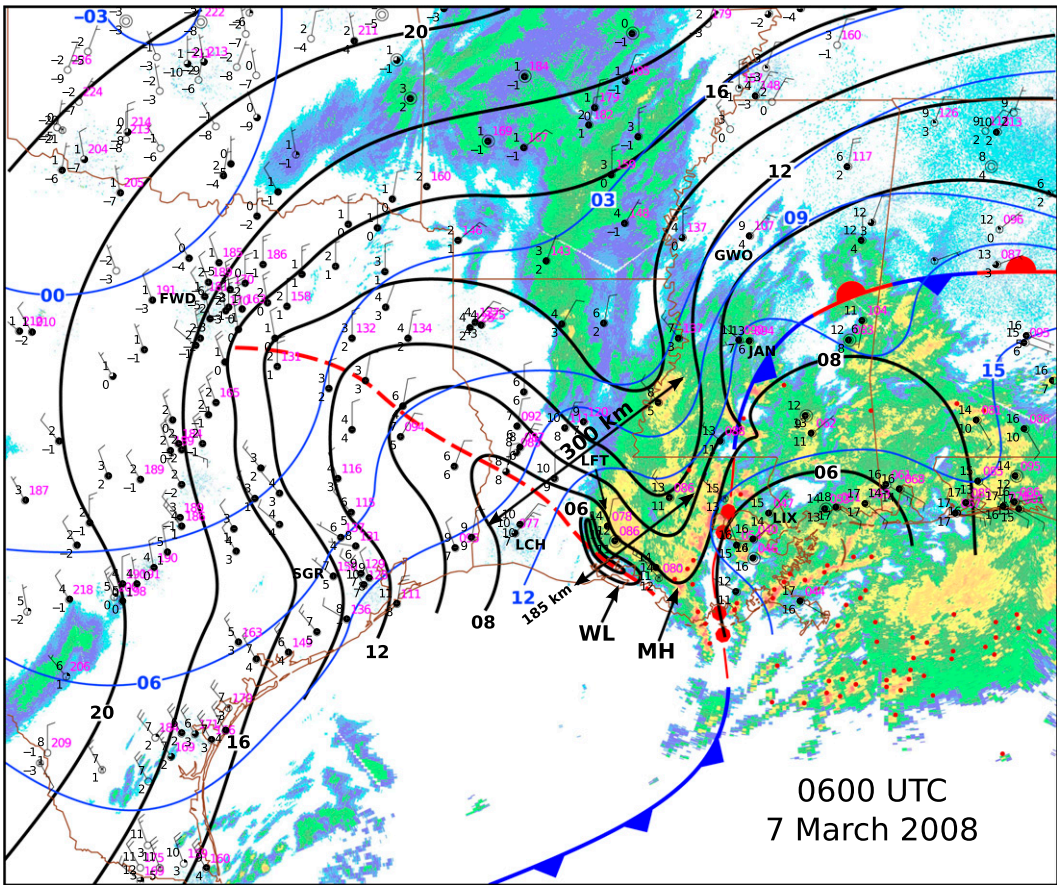

FIG. 8. As in Fig. 6, but for 0600 UTC 7 Mar (see Fig. 6 for reflectivity color bar). "WL" and "MH" denote the wake low and mesohigh (respectively), as in Figs. 5c,d.

(over 1.5 h) closely matches the maximum pressure change in Fig. 8 along a northeast–southwest transect across LFT and the MCS. Close correlation between p' and u' is observed.

The rapid p' fall and subsequent recovery at LFT occur over ~20 min around 0630 UTC as the wind backs from northeasterly to northwesterly, gusts reach 14 m s^{-1}, and rainfall ceases, consistent with WL passage (Fig. 5d). This feature resembles WL passage at LCH (~0430 UTC; Fig. 5c) in terms of pressure, wind, and precipitation relationships, though it is clearly a much higher amplitude and more rapid pressure fall. It is plausible that a WL situated at the back edge of the MCS stratiform region, as indicated in the time series at LCH (Fig. 5c), intensified as the MGW caught up and became collocated with the WL. This collocation would result in stronger subsidence within the strongly stratified environment behind the cold front, and hence a more intense surface pressure reduction (Figs. 5d and 6).

Since squall-line MH–WL couplets propagate largely in accordance with the dynamics of hydrostatic gravity waves, the p'–u' relationship within these features is analogous to that of a MGW (Johnson and Hamilton 1988; Loehrer and Johnson 1995; Haertel and Johnson 2000). Hence, the MGW- and MCS-related flow and pressure signatures cannot be readily separated in the vicinity of the MCS at this point since these features are largely collocated (Fig. 8).

The 1200 UTC sounding from LIX (Fig. 7c) exhibits a ~200-hPa-deep stable layer. This stable layer is evidently supportive for ducting the MGW, with $D > D_{\text{crit}}$ (Table 1). While C_d^* is 38% larger than $\overline{C^*}$, it is not clear if (2) is accurate in the presence of diabatic heating, which might be important for the propagation of the MGW in this region. The overlying layer exhibits steep lapse rates and contains a critical level with reduced Ri at ~550 hPa, suggesting that the reflection of wave energy is supported.

c. *Maintenance*

A mesoanalysis for 0900 UTC (Fig. 9) shows that the squall line that was closely tied to the leading edge of the

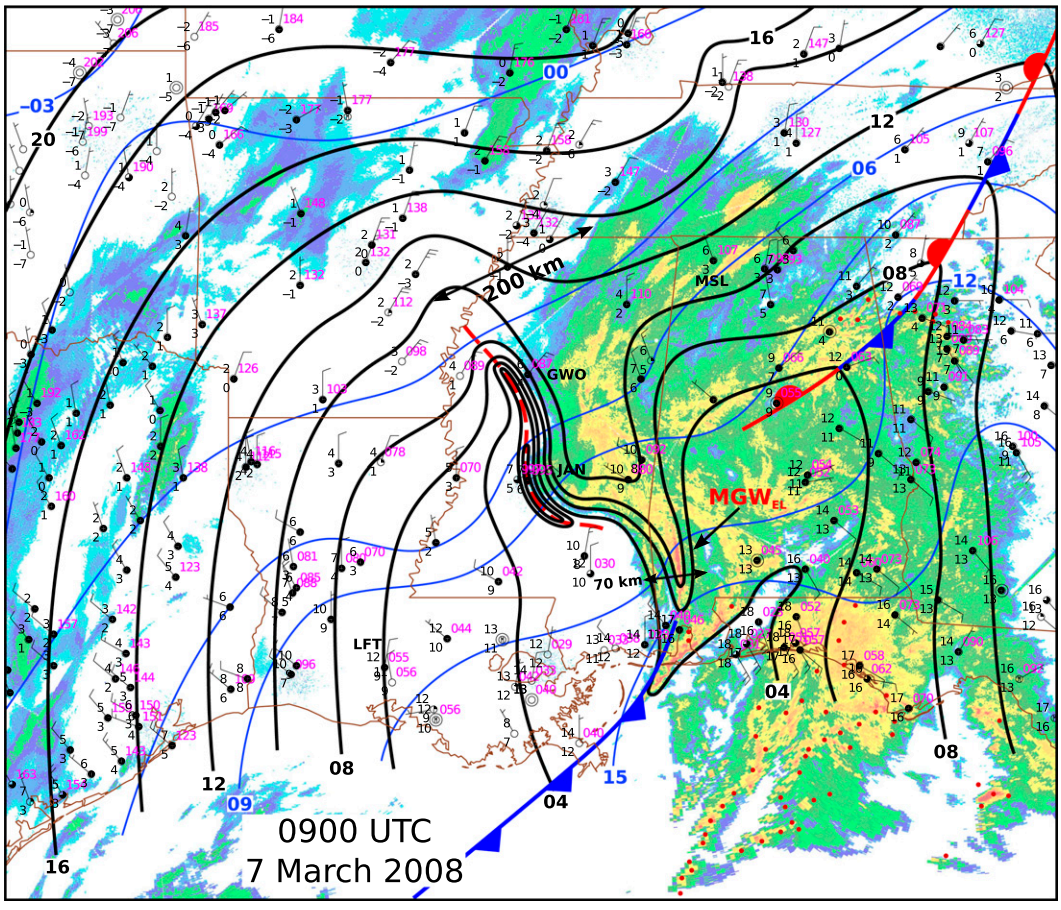

FIG. 9. As in Fig. 6, but for 0900 UTC 7 Mar. MGW_{EL} is indicated.

MH from 0300 to 0600 UTC has all but disappeared (Figs. 6 and 8), and deep convection (as indicated by CG lightning flashes) is confined mostly to the warm sector in the GoM coastal region and offshore. A stratiform rain shield spans much of MS and AL, the back edge of which is marked by a sharp SLP minimum. Reflectivity values are slightly enhanced within the ridge leading the trough. A loop of mosaic base reflectivity indicates coherent evolution of this stratiform rain shield and continuity of its sharp back edge from 0600 to 0900 UTC (http://johnson.atmos.colostate.edu/~ruppert/MGW_7M08/).

The temperature and pressure fields at 0900 UTC differ from those at 0600 UTC in several key ways (Figs. 8 and 9). An axis of cooler temperatures no longer appears within the inverted ridge leading the trough at 0900 UTC. The trough–ridge couplet no longer extends far beyond the rain shield. A sharp closed low, which is akin to the WL at 0600 UTC, now spans approximately half the meridional extent of MS in connection with the larger stratiform rain shield. And last, the wavelength of the trough–ridge couplet is now ~200 km, which is similar to the wavelength of the MH–WL couplet of 0600 UTC. Taking $c = \lambda/T$ and assuming $T \sim 2$ h (Fig. 5e), yields $c \sim 25\ \mathrm{m\,s^{-1}}$ (closely matching c calculated from MGW isochrones; Fig. 1).

The evolution from the broad MGW trough–ridge couplet of 0600 UTC to a sharper couplet predominately tied to the stratiform precipitation shield suggests that the MGW's maintenance is now governed largely by coupling with the precipitation (Figs. 8 and 9). Not coincidentally, a MH–WL couplet can be understood as the gravity wave response to the diabatic forcing by the stratiform region (i.e., low-level cooling; Johnson and Hamilton 1988; Loehrer and Johnson 1995; Haertel and Johnson 2000). Hence, the intense pressure couplet at 0900 UTC is analogous to an extensive MH–WL couplet (Fig. 9). The lack of an axis of cooler surface temperatures at 0900 UTC indicates that the cooling is aloft, therefore corroborating that the pressure couplet's propagation is governed by gravity wave motions in contrast the motions of a density current (Haertel et al. 2001).

While the trough–ridge couplet in central–northern MS exhibits characteristics of a wave of depression, the stratiform rain shield along the southern MS–AL border is marked by a wave of elevation (i.e., MGW_{EL}), with an associated SLP 4-hPa ridge sitting within an area of sharply enhanced reflectivity values. A discussion of this MGW_{EL} is provided in section 5.

MGW passage in the meteogram for Jackson (JAN; Fig. 5e), MS, qualitatively resembles that at LFT (Fig. 5d), although in contrast to LFT, a pronounced rainfall burst does not coincide with the westerly wind shift when p' begins to rise; rather, a lesser burst in rainfall occurs during the period of high pressure preceding the rapid p' fall. Similar to JAN, minimal rainfall at Greenwood (GWO; Fig. 5f), MS, only appears in connection with the area of enhanced stratiform rainfall centered within the inverted ridge (Fig. 9). This apparent lack of deep convection and a well-defined gust front is consistent with the dominance of gravity wave dynamics in the propagation of the precipitation system (Figs. 6 and 8; Haertel et al. 2001).

The overall p'–u' evolution at JAN and GWO very closely resemble that at LFT, particularly in the rapidity of p' and u' changes (Figs. 5d–f). Amplification of the intense pressure fall evidently occurs subsequent to its passage through LFT, as the p' fall increases from ~10 hPa at LFT to ~12 hPa at GWO, with the majority of the fall at GWO occurring within 45 min (Figs. 5d,f). The 12-hPa p' fall at GWO includes an ear-popping crash of 6.7 hPa in 10 min, with a dramatic increase in northeasterly flow as gusts reach 20 m s^{-1} (6 m s^{-1} greater than those at LFT during trough passage). The associated change in u' during trough passage at GWO is ~17 m s^{-1} over 25 min.

The sounding profile for JAN (Fig. 7d) closely resembles that at LIX (Fig. 7c), with a deep inversion and an overlying conditionally unstable layer, and a critical level with reduced Ri within the overlying unstable layer. The ducting parameters in Table 1 demonstrate that the observed wave duct was geometrically suitable for the MGW, and that C_d^* for the observed stable layer matches $\overline{C^*}$ to within ~2 m s^{-1}.

At Muscle Shoals (MSL; Fig. 5g), AL, a large decrease in p' and u' ($\Delta p' \sim 11$ hPa and $\Delta u' \sim 8$ m s^{-1}) occurs in two stages with a brief plateau near 1200 UTC as rainfall ends. In contrast to the LCH, LFT, JAN, and GWO meteograms (Figs. 5c–f), no leading p' increase is observed. Light rainfall begins around 0800 UTC, increases in intensity through the start of the first p' decrease, and then abruptly ceases at the p' plateau (Fig. 5g). Wind gusts increase as rainfall reaches a final peak before ceasing, and they reach ~17 m s^{-1} during passage of the p' minimum. The meteogram for Nashville (BNA; Fig. 5h), TN, depicts similar p', u', and rainfall evolution, with a two-step decrease in p' followed by a very rapid ~8-hPa rise. At BNA, light northerly winds veer to northeasterly and increase to ~12.5 m s^{-1} for approximately 1 h prior to the p' minimum as rainfall ceases, before backing to northwesterly during and following the abrupt p' recovery (Fig. 5h).

The 1200 UTC mesoanalysis (Fig. 10) is qualitatively similar to the 0900 UTC mesoanalysis (Fig. 9). No CG lightning flashes are found near the leading inverted ridge, suggesting little-to-no accompanying deep convection. Rainfall is very clearly enhanced within the inverted ridge, consistent with the rainfall time series at JAN, GWO, MSL, and BNA (Figs. 5d–h), which reflects enhanced lifting where pressure is increasing (the lack of a p' increase as rainfall intensifies at BNA and MSL is likely due to the northeastward motion of the MGW; Fig. 10). The stepwise decrease in pressure at MSL is reflected in the pressure gradient near the trailing edge of the rain shield in the separation between the 1006- and 1004-hPa isobars; rain ends abruptly in the weak pressure gradient region between the two concentrated fall areas (Figs. 5g and 10).

Base reflectivity and velocity images are presented for 1140 UTC from Columbus Air Force Base (GWX), MS, in Fig. 11. Several pronounced reflectivity bands (>50 dBZ) are evident: two along the northern rain shield edge near MSL (“B1” and “B2”), which are parallel, and one along the northwest–southeast-oriented rain shield edge to the south (“B3”). The cross section indicates that the heavy precipitation cores in B1 and B2 only extend to ~3 km, with reflectivity values decreasing rapidly above this level, corroborating that there is little-to-no deep convection accompanying the MGW at this stage. At 1140 UTC, MSL sits in a local maximum of outbound velocity values, which stretches south-southeastward within B1. Outbound velocities reach 20 m s^{-1}, adjacent to areas of 15 m s^{-1} inbound velocities at the rain shield edge. This differential velocity signal, which is persistent (not shown), reflects the strong low-level divergence connected with rapid sinking motion and rainfall shutoff (consistent with u' and the total wind vectors at MSL; Fig. 5g).

The 1200 UTC vertical sounding profile for BNA (Fig. 7e; shortly preceding the MGW passage) depicts a ~325-hPa-deep layer of weak-to-moderate stability. In connection with such a deep stable layer, C_d^* is ~50% larger than $\overline{C^*}$ (Table 1). A critical layer is embedded within an overlying moist adiabatic layer, suggesting favorable conditions for wave reflection; however, Ri > 1 throughout most of this layer. The impact of this complex stratification pattern (i.e., with multiple distinct inversions) on the character of wave ducting is unknown.

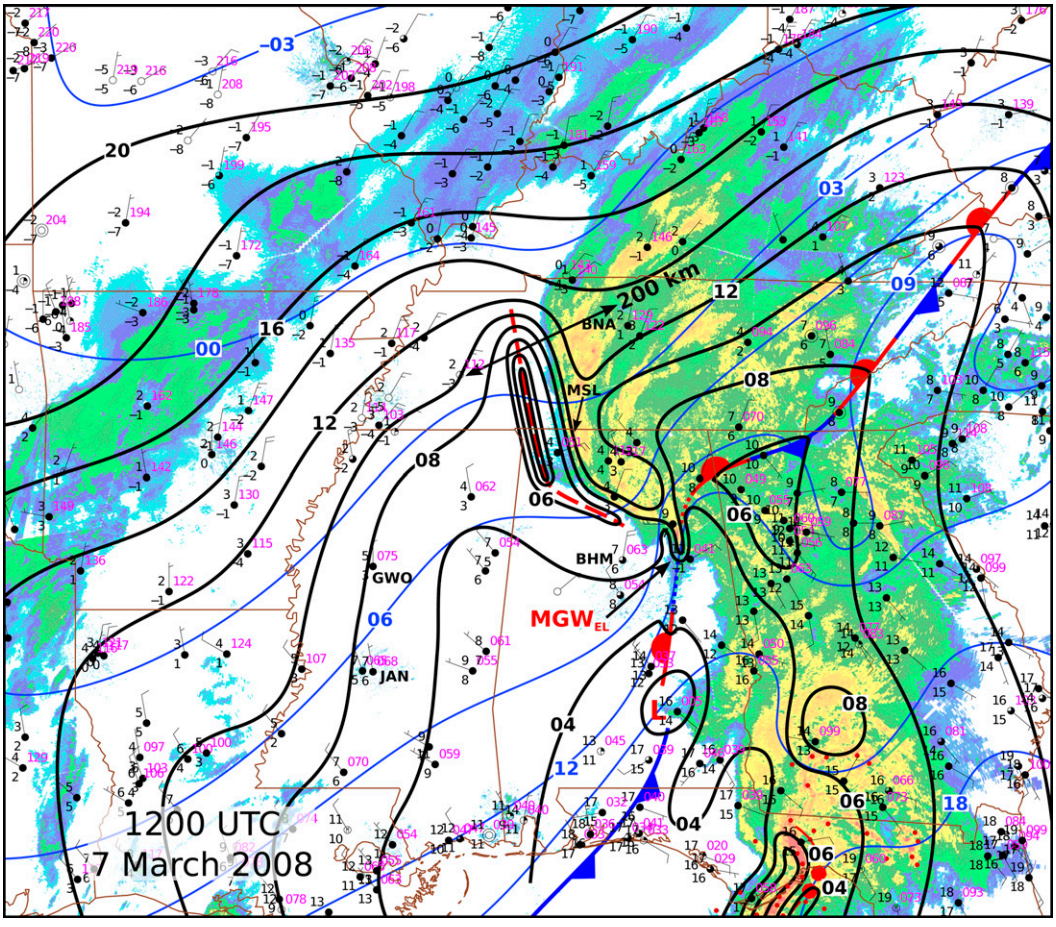

FIG. 10. As in Fig. 6, but for 1200 UTC 7 Mar. MGW_{EL} is indicated.

d. Dissipation

A surface mesoanalysis for 1500 UTC (Fig. 12) shows that the stratiform rain shield has lost its sharp trailing edge and much of the embedded banded structure since 1200 UTC (Figs. 10 and 11). Furthermore, the inverted trough–ridge couplet of 1200 UTC (Fig. 10) is virtually unidentifiable, with the MGW now being comprised mostly by a weak, shorter-wavelength inverted trough with dual-peak structure. The meteogram for Lexington (LEX; Fig. 5i), KY, depicts a p' and u' evolution that resembles that at VCT and SGR (Figs. 5a,b): northeasterly flow ($u' < 0$) and gustiness both increase as p' begins to decrease, and p' exhibits a two-step decrease (consistent with Fig. 12). In contrast to MGW passage at MSL and BNA, rainfall does not exhibit a marked increase and shutoff in advance of and during the p' decrease (Figs. 5g–i).

The 1800 UTC mesoanalysis (Fig. 13) depicts an even more amorphous stratiform shield, with greater precipitation in the wake of the MGW than any prior times (Figs. 6, 8–10, and 12). The MGW has lost amplitude since 1500 UTC (Fig. 12). The meteogram for Wilmington (ILN; Fig. 5j), Ohio (OH), indicates that the MGW is barely detectable at this time above other background noise in the p' and u' time series. Wind gusts do not substantially increase, although rainfall intensity increases slightly with MGW trough passage, which is marked by a <1 hPa p' decrease that occurs over about 1 h.

The vertical profile for ILN depicts a 445-hPa-deep stable layer (Fig. 7f). Similar to BNA (Fig. 7e), C_d^* greatly exceeds $\overline{C^*}$ in connection with this deep layer. A critical level is situated near a shallow inversion around 500 hPa, beneath a layer of moist-neutral stability. As at BNA (Fig. 7e), the impact of such complex vertical thermodynamic structure on wave ducting is unclear.

5. Short-lived wave of elevation

Following the period in which the main MGW (wave of depression) amplified as it interacted with a MCS MH–WL

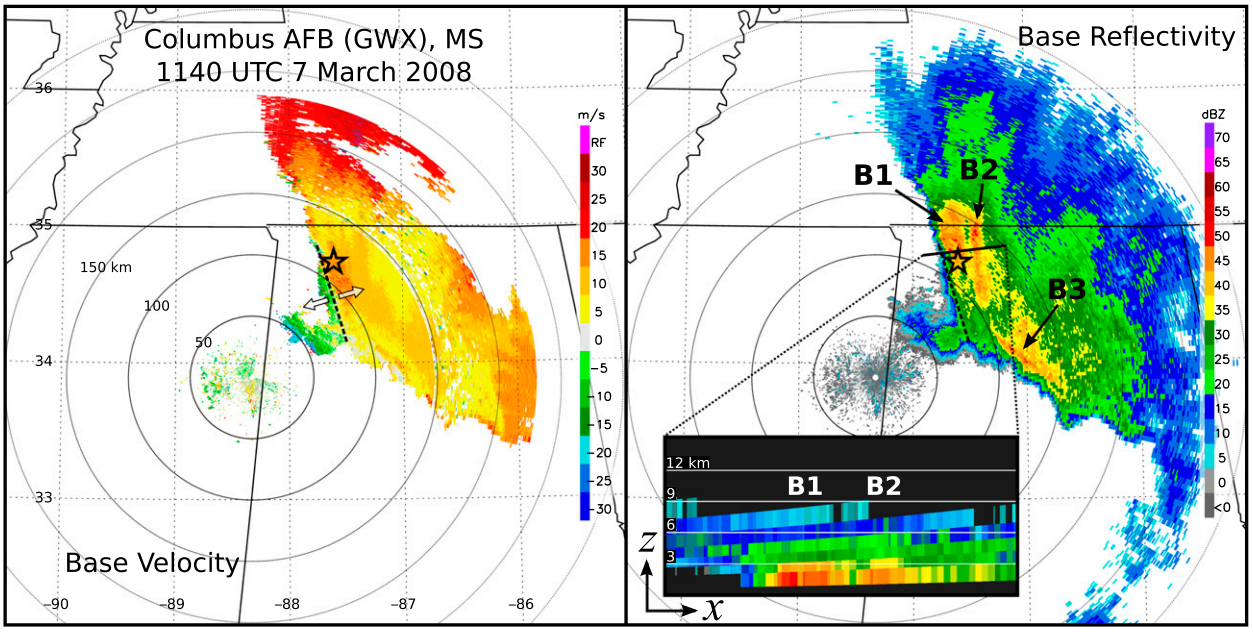

FIG. 11. Maps of (left) 0.48° base radar velocity and (right) reflectivity for 1140 UTC 7 Mar from Columbus Air Force Base (GWX), MS. Range rings are shown every 50 km. The dashed line and two arrows in the left panel indicate the inferred low-level diffluence. B1, B2, and B3 denote three rainbands referred to in the text. The star denotes the location of MSL (Fig. 5g). The solid line in the right panel denotes the transect of the embedded reflectivity cross section (vertical axis is height, in km).

couplet around 0600 UTC (Fig. 8), the eastward-propagating MGW_{EL} developed within the remnants of the MCS squall line (http://johnson.atmos.colostate.edu/~ruppert/MGW_7M08/). Meteograms along the path of the MGW_{EL} are provided in Fig. 14, which include temperature and dewpoint temperature (note the larger precipitation scale). At New Orleans (NEW; Fig. 14a), LA, a rapid p' rise and fall of 4 hPa occurs over 1 h, which comes with a wind shift from easterly to strong northwesterly–northerly flow. A burst of intense rainfall coincides with maximum p' (i.e., more intense than during squall-line passage at LFT; Fig. 5d). There is an increase in u' of $10\,m\,s^{-1}$ during the increase in p' as gusts exceed $25\,m\,s^{-1}$, which is followed by a rapid decrease with the decrease in p'.

The 2°C temperature drop as MGW_{EL} passes is consistent with its collocation with the frontal baroclinic zone (Fig. 9). While a temperature drop suggests possible interpretation as a density current, p' would be expected to remain high following the wind shift for a pure density current, whereas it instead returns to its approximate previous value. The correlation between p' and u' suggests gravity wave propagation. MGW_{EL} is dominated by rising motion and moist adiabatic cooling (i.e., a wave of elevation), whereas the primary MGW is dominated by sinking motion and adiabatic warming (i.e., a wave of depression; Figs. 5 and 14a).

Several base reflectivity maps and cross sections of reflectivity and storm-relative velocity (SRV) are provided in Fig. 15 for analysis of MGW_{EL}. While the stratiform rain shield in northern LA exhibits a sharp trailing edge oriented from northwest–southeast in association with the primary MGW (Figs. 8 and 9), the more striking feature in Fig. 15a is the very sharp, intense south–north-oriented rainband, which moves due eastward with northward translation (cf. link provided earlier in this section). According to the NEW times series and the 0900 UTC surface analysis, this rainband is centered within the MGW_{EL}, which is manifest as a narrow inverted SLP ridge with wavelength ~70 km (Figs. 9 and 14a). This pressure–rainfall relationship is consistent with locally enhanced rising motion within MGW_{EL}. Cross sections across the rainband reveal a forward-tilted high-reflectivity (i.e., >50 dBZ) core extending up to ~3 km, which is connected to a 3-km-deep pronounced couplet of confluence beneath diffluence (Figs. 15b,c). This confluence–diffluence structure corroborates the presence of locally enhanced rising motion, and is consistent with the wind barbs and u' time series for NEW (Fig. 14a). Reflectivity values are notably lower immediately in advance of the rainband, suggestive of leading subsidence warming (Figs. 15a–c). SRV magnitudes of 5–$10\,m\,s^{-1}$ in the low-level westerly stream behind the rainband are consistent with the $25\,m\,s^{-1}$ gusts (adding storm motion) and the coinciding wind shift to northwesterly flow at NEW (Figs. 14a and 15a–c).

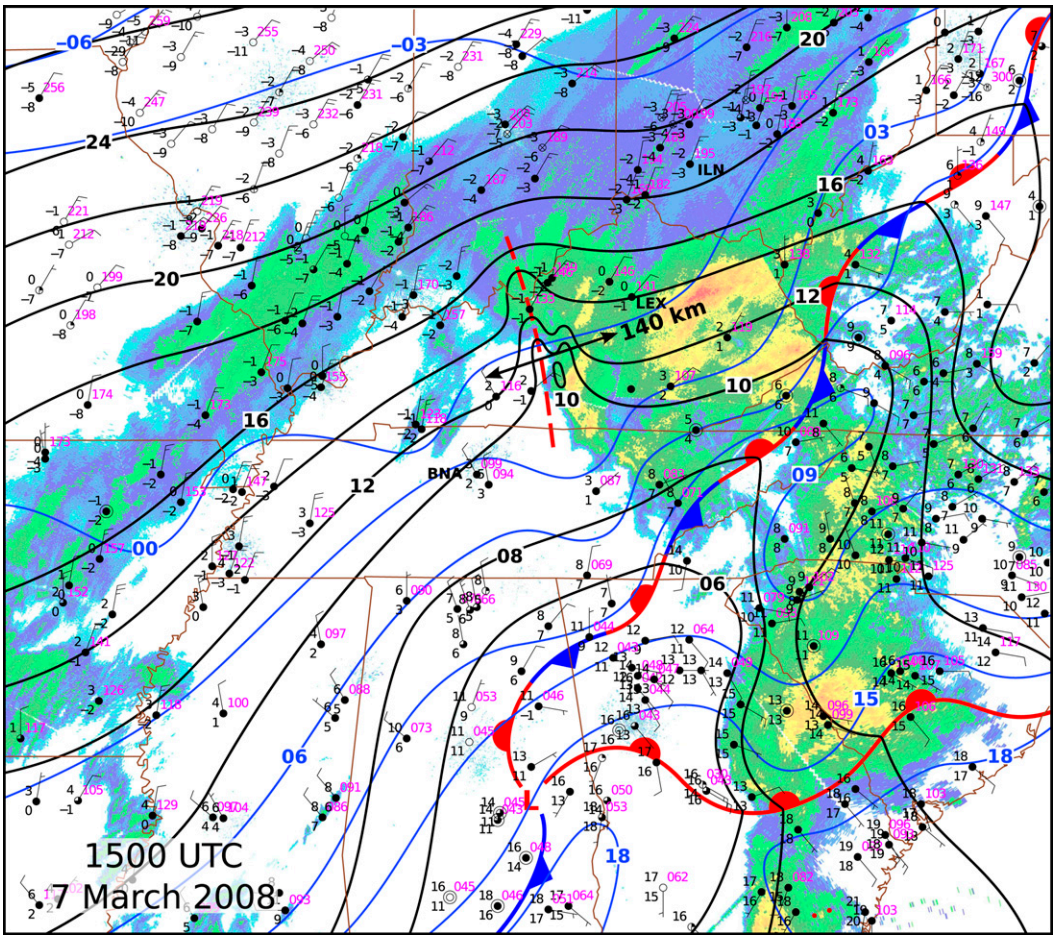

FIG. 12. As in Fig. 6, but for 1500 UTC 7 Mar.

While these cross sections resemble depictions of a density current with a leading rainband (Figs. 15b,c), the rainfall–pressure relationship and p'–u' correlation during passage of MGW_{EL} indicate that it is a solitary gravity wave of elevation coupled with enhanced rainfall and moist adiabatic cooling (Fig. 14a). It is plausible that latent heating within this rainband is augmenting the lifting, and hence maintaining the MGW_{EL}, via the wave–CISK mechanism (Lindzen 1974; Raymond 1984). Previous studies have described similar solitary MGWs as formed in response to a density current propagating through a stable air mass (e.g., Christie et al. 1979; Ramamurthy et al. 1993; Koch et al. 2008).

The time series for Mobile Downtown Airport (BFM; Fig. 14b), AL, depicts very different evolution from that at NEW (Fig. 14a). A 2°C increase in temperature follows a steady local moistening, followed by several bursts of very heavy rainfall [i.e., 6–8 mm $(5\,\text{min})^{-1}$ or 72–96 mm h^{-1}] separated by 30–45 min. An increases in p' of ~1 hPa occurs leading up to each burst of rainfall, followed by a rapid p' decrease during the rainfall. A map of reflectivity at 0805 UTC demonstrates that the rainfall bursts at BFM are caused by the passage of multiple individual cells (Figs. 14b and 15d). It is possible that small-scale gravity waves propagating ahead of the more intense MGW_{EL} and gust front are partly responsible for this periodic organization of cells (i.e., note the correlation between u' and p'; Figs. 14b and 15d; Ralph et al. 1999). A cross section across one of these cells depicts a core of high reflectivity extending up to ~5 km, indicating much deeper convection and greater convective instability (Fig. 15e). The cross sections depict strong approximately southerly vertical wind shear, with an indication of a bounded weak echo region (BWER; Lemon and Doswell 1979) above an area of low-level confluent flow (Figs. 15e,f). This feature, together with the high-reflectivity appendage resembling a hook echo (Fig. 15d), is indicative of the presence of a supercell with a rotating updraft.

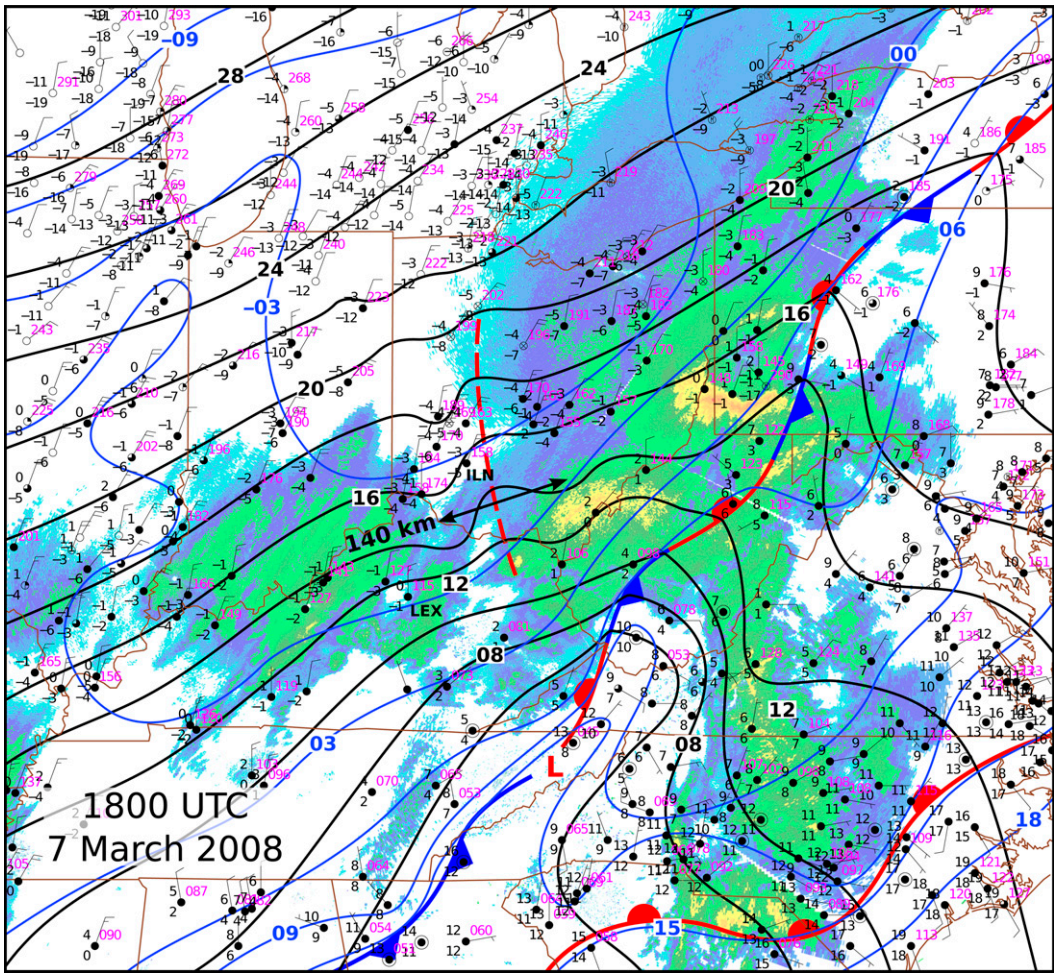

FIG. 13. As in Fig. 6, but for 1800 UTC 7 Mar.

The major wind shift at BFM around 0900 UTC does not coincide with the passage of a rainband or a strong wave in p', indicating that MGW_{EL} does not make it to BFM (Figs. 9 and 14b). However, there is evidence of MGW_{EL} passage at Birmingham (BHM; Fig. 14c), AL. The MGW_{EL} passage at BHM qualitatively resembles that at NEW, with a rapid p' increase, a coinciding u' increase, followed by very rapid p' and u' falls (Figs. 14a,c). The magnitude of p' change at BHM with the MGW_{EL} passage is ~6 hPa. The temperature decreases by 2°C with the MGW_{EL} passage, similar to the MGW_{EL} passage at NEW. The MGW_{EL} rapidly decays after passing BHM (Figs. 10 and 11).

The lack of a MGW_{EL} at BFM and the indication of vigorous deep convection there (Figs. 14b and 15d–f) suggests that the low-level stability in this warm sector environment is too weak to provide a suitable wave duct for the MGW_{EL}. The MGW_{EL} readily continues northeastward after passing through NEW, however, remaining attached to the front and on the north side of the surface cyclone where wave ducting is better supported (Figs. 1, 3b,c, 9, 10, and 14a–c). The MGW_{EL} rapidly dissipates around 1200 UTC when the front becomes stationary (Figs. 1 and 10).

6. Discussion

a. Genesis

Analysis of ASOS data suggests that the MGW (wave of depression) originated in the vicinity of northern Mexico (Figs. 1 and 5). Organized deep convection was confined to the unstable GoM air mass (Figs. 3, 4, and 6), suggesting that convection did not play a role in MGW genesis. Evidence points strongly to the surface cold front as the primary genesis agent. Ralph et al. (1999, see their Fig. 23) showed that gravity waves can be excited by cold fronts as follows: when the cross-front, front-relative overriding flow ($\mathbf{V}_r$) becomes sufficiently strong (~20 m s^{-1}), thermal wind balance is broken, the overriding flow becomes perturbed, and a deep gravity wave is

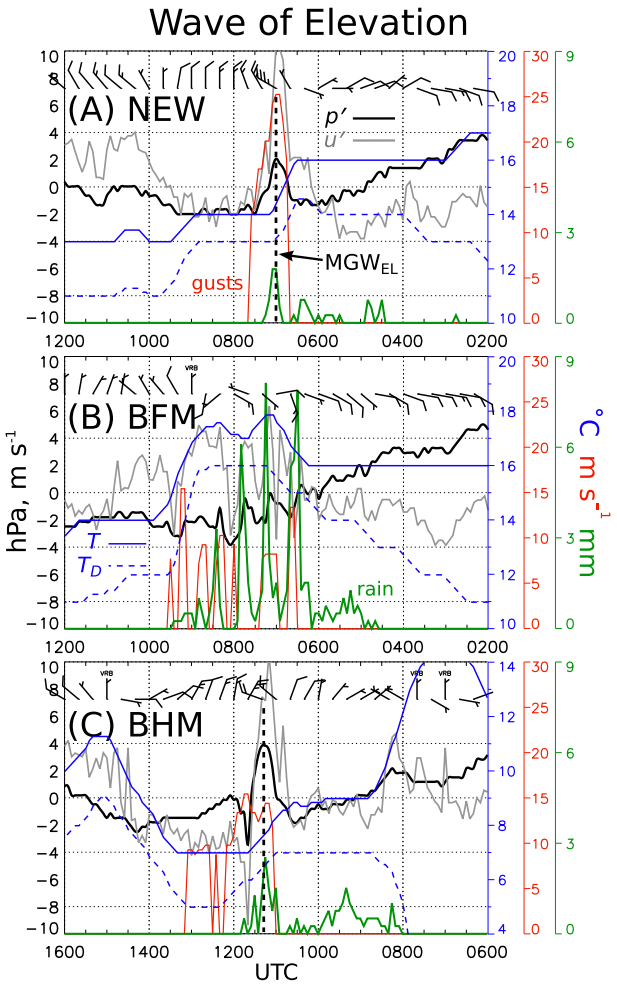

FIG. 14. Meteograms for the secondary MGW, characterized by a wave of elevation (MGW$_{EL}$). As in Fig. 5, but with T and T_d included (blue solid and dashed lines, respectively; °C; blue ordinate scale), and for (a) New Orleans (NEW), LA; (b) Mobile Downtown Airport (BFM), AL; and (c) Birmingham (BHM), AL. The black vertical dashed line indicates MGW$_{EL}$, which did not pass through BFM. Note that the precipitation scale goes up to 9 mm (cf. 3 mm in Fig. 5).

excited that can then propagate independent of the cold front if conditions support wave ducting.

To assess the possible role of the cold front in gravity wave genesis in the present case, maps of RUC-derived 600-hPa vertical pressure velocity ω and surface θ are provided alongside vertical cross sections across the surface cold front for several times on 6 and 7 March (Figs. 16 and 17). The cross sections include frontogenesis F, which is calculated as follows (neglecting diabatic heating and tilting; Petterssen 1936, 1956):

$$F = \frac{|\nabla_h \theta|}{2}[\mathrm{def}(\mathbf{u})\cos 2\beta - \delta], \qquad (4)$$

where def is the total deformation of the horizontal flow ($\mathbf{u}$), β is the angle between isentropes and the axis of dilatation, δ is horizontal divergence, and the subscript h indicates horizontal derivatives. At 1800 UTC 6 March, mostly weak baroclinic zones surround Mexico's high terrain in connection with elevated surface heating, with a stronger baroclinic zone to the north associated with the advancing cold front (Figs. 16a and 17a). As the front pushes into and around Mexico's steep slopes by 2100 UTC 6 March, extensive ω couplets appear that hug the terrain (Fig. 16b). The cold front is characterized by frontogenesis, a low-level wind shift from northwesterly to stronger (>16 m s^{-1}) northerly flow across the frontal baroclinic zone, and CAA as indicated by flow backing across the frontal stable layer (Figs. 16b and 17b).

Comparison of Figs. 16b and 17b demonstrates that the terrain-hugging ω couplets in Fig. 16b are part of a deep, vertically propagating gravity wave, which has its vertical velocity peaks near and just above the surface cold front (this structure has little sensitivity to the exact transect endpoints). This gravity wave closely resembles the frontally generated gravity waves described by previous studies (Snyder et al. 1993; Ralph et al. 1999; Zhang and Koch 2000; Plougonven and Snyder 2007). Since frontal motion near the ω couplet in this case is ~14 m s^{-1} toward ~205° (Fig. 16b), and the mean frontal overriding flow from ~800 to 600 hPa is ~15 m s^{-1} from ~265° (Fig. 17b), $\mathbf{V}_r$ is ~22 m s^{-1}. The leading edge of the front is 1.5–2 km deep (Fig. 17b). These values are consistent with those of Ralph et al. (1999), suggesting that the cold front in the present case was able to excite a deep gravity wave through the flow obstacle effect.

Another possibly relevant puzzle piece in the MGW genesis process is the appearance of localized peaks in vertical motion and frontogenesis near the exit region of the upper-level jet streak (~300 hPa) from 2100 to 2300 UTC 6 March, which connect with the deep, surface-based frontal gravity wave (Figs. 2a and 17b,c). These peaks might signify gravity wave emission (or growth) in response to flow imbalance as air parcels decelerate through the jet streak exit region (Zhang 2004; Snyder et al. 2007, 2009; Wang et al. 2009; Wang and Zhang 2010; Plougonven and Zhang 2014). Whether this stratospheric gravity wave energy source was able to communicate with the lower troposphere, however, is unclear.

From 1800 UTC 6 March to 0000 UTC 7 March, a critical level descends into the midtroposphere and progresses northeastward with the advancing upper-level trough and jet streak, and midtropospheric static stability decreases in connection with the arrival of steep-lapse-rate air (Figs. 2a, 7a, and 17), indicating

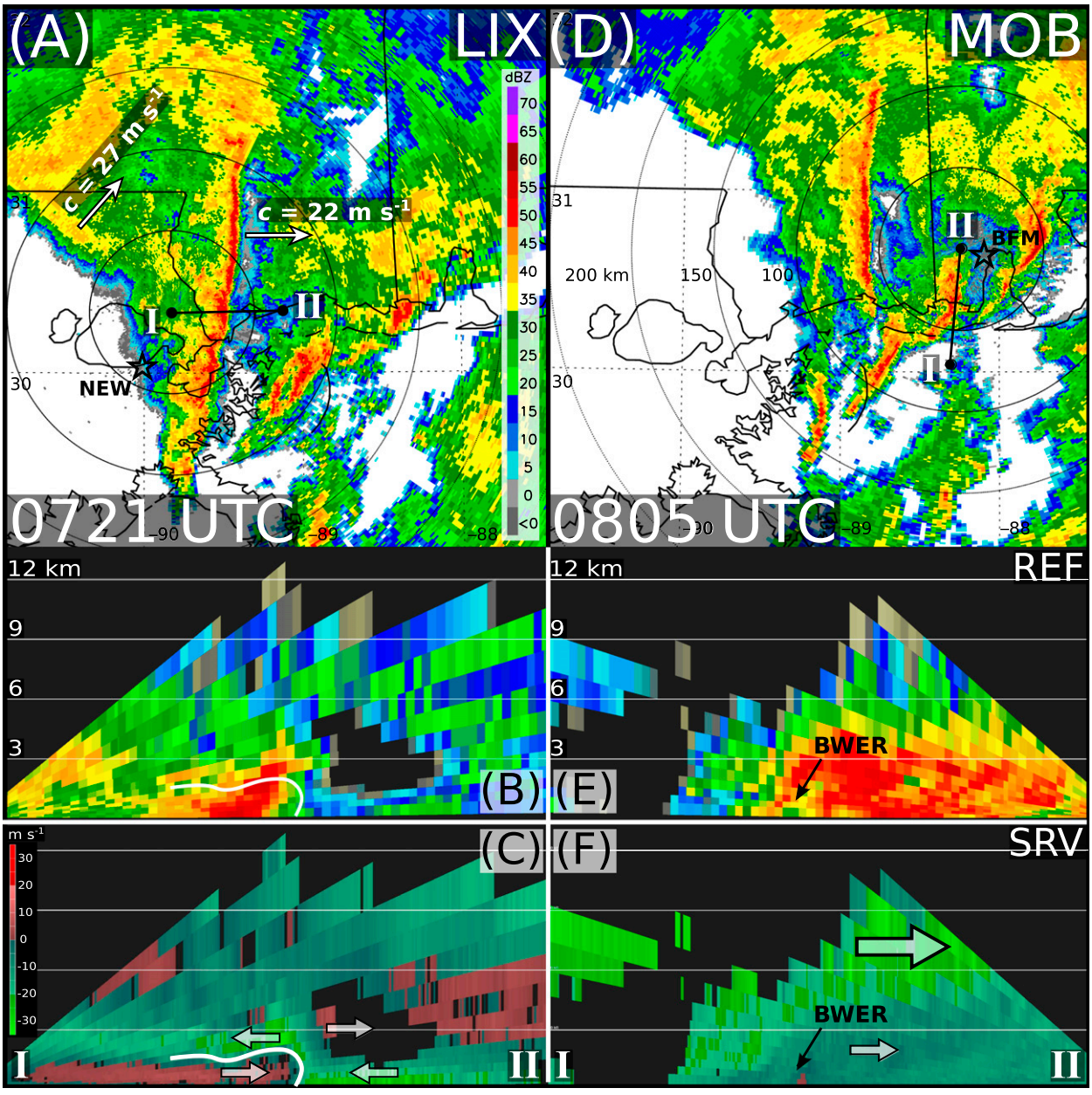

FIG. 15. A map of (a) base reflectivity and cross sections of (b) reflectivity and (c) storm relative velocity (SRV) for 0721 UTC 7 Mar from Slidell (LIX), LA. (d)–(f) As in (a)–(c), but for 0805 UTC 7 Mar from Mobile (MOB), AL. SRV is calculated using the eastward-directed storm motion vector of 22 m s^{-1} shown in (a). The motion of a rainband leading the primary MGW (northeastward directed) is also indicated in (a). Transects for the cross sections are indicated in (a) and (d). "BWER" denotes a possible bounded weak echo region. The white curve in (b) and (c) separates negative SRV values from the area of positive values. The white arrows in (c) and (f) highlight the inferred flow direction. Meteogram station locations (for Fig. 14) are indicated.

more conducive conditions for wave ducting. Near the northeastern edge of the transect at 0000 UTC, the stable layer spans ~950–725 hPa, or ~2.2 km (Fig. 17d). This value, which approximately equals D_{crit} at CRP (Table 1), is consistent with deeper cold air inland from CRP (Fig. 1). Taking $\overline{\theta}$ and $\Delta\theta$ from the CRP sounding yields C_d^* ~24 m s^{-1}, which matches $\overline{C^*}$ at CRP to within ~2 m s^{-1} (Table 1). These calculations indicate that conditions became suitable for wave ducting by 0000 UTC and that the frontal gravity wave was able to propagate independent of its genesis source, as has been documented by previous studies (Ralph et al. 1999; Zhang and Koch 2000; Knippertz et al. 2010).

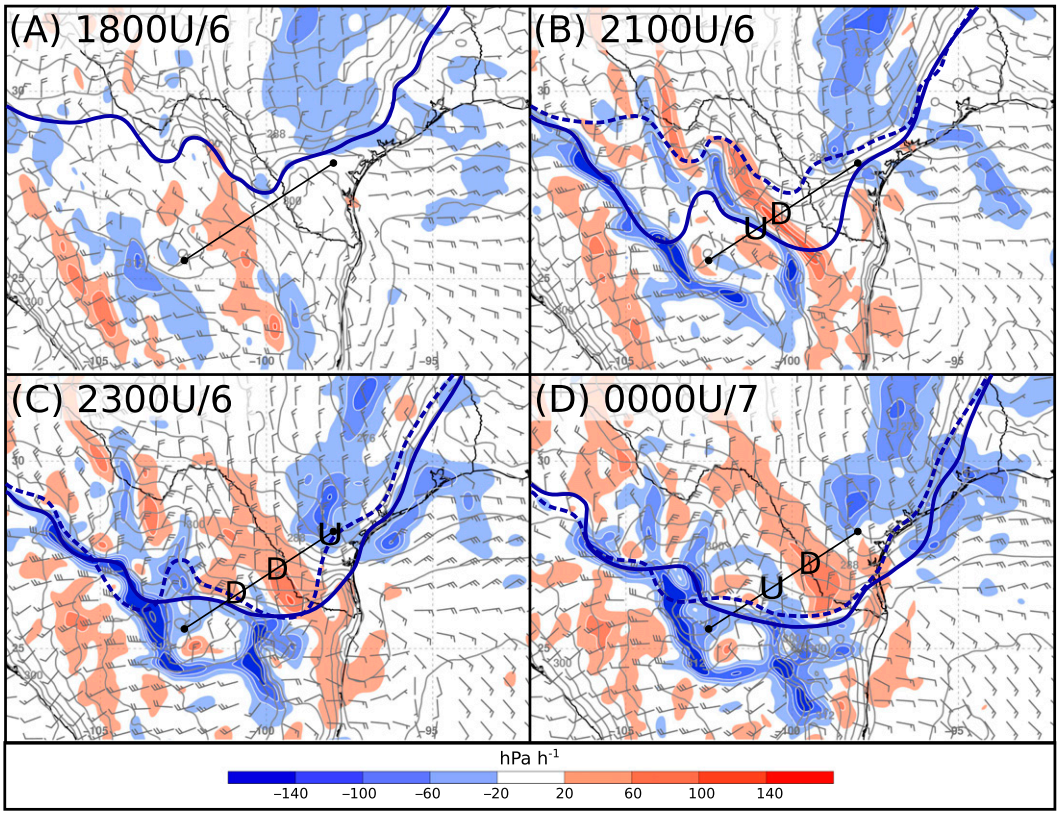

FIG. 16. Maps of 600-hPa vertical pressure velocity ω (shaded according to the color bar; hPa h^{-1}), 2-m potential temperature θ (thin contours; K), and 10-m wind (barbs; format is as in Fig. 2) from the (a) 1800, (b) 2100, and (c) 2300 UTC 6 Mar, and (d) 0000 UTC 7 Mar 13-km Rapid Update Cycle (RUC) analyses. Blue lines denote the position of the surface cold front, and the dashed lines are frontal position at the preceding time. The straight, solid line denotes the transect for Fig. 17; "U" and "D" highlight several regions of upward and downward motion, respectively, that correspond with those in Fig. 17.

The RUC depicts areas of upward and downward motion that appear to emanate from the region of the frontal gravity wave, widen, and shift northeastward from 2100 UTC 6 March to 0000 UTC 7 March (Figs. 16 and 17). These features, however, do not propagate as a ducted MGW, which should exhibit a vertical half-wavelength of approximately $2 \times D$ (~4 km; Table 1) and signals in vertical motion that maximize near or within the lower-tropospheric inversion (RCV93). Therefore, while the RUC identifies the likely gravity wave genesis mechanism, it does not properly depict the evolution from the incipient gravity wave to a ducted MGW. For this reason, the amplification of surface pressure anomalies associated with MGW–MCS coupling around 0600 UTC was missed by the RUC (Figs. 3 and 8). Previous mechanistic studies of the pressure and circulation response to MCS diabatic processes, however, offer a possible explanation of MGW amplification in the present case, as described next.

b. *Amplification and maintenance*

Prior to any connections with rainfall, the MGW was characterized by a wavelength of ~300 km, with surface pressure falls of ~4 hPa accompanying its passage (Figs. 5a–c and 6). Its wavelength later decreased by ~100 km and surface pressure falls increased to >10 hPa after it became coupled with a MCS (Figs. 4c–e, 5d–h, 6, and 8–10).

The initial MGW amplification around 0600 UTC owed to the diabatic forcing of the MCS, which caused development of a small-scale mesohigh–wake low (MH–WL) couplet within the MCS stratiform precipitation region and the broader MGW trough–ridge couplet (Fig. 8). MH formation was indicated from 0300 to 0600 UTC by amplification of a SLP ridge as a cold tongue appeared within the stratiform region (the MH, however, was not clearly distinguishable from the broader MGW inverted ridge; Figs. 5c,d, 6, and 8). A WL appeared as a sharp low pressure center at the immediate trailing edge of the stratiform region, the passage of which was

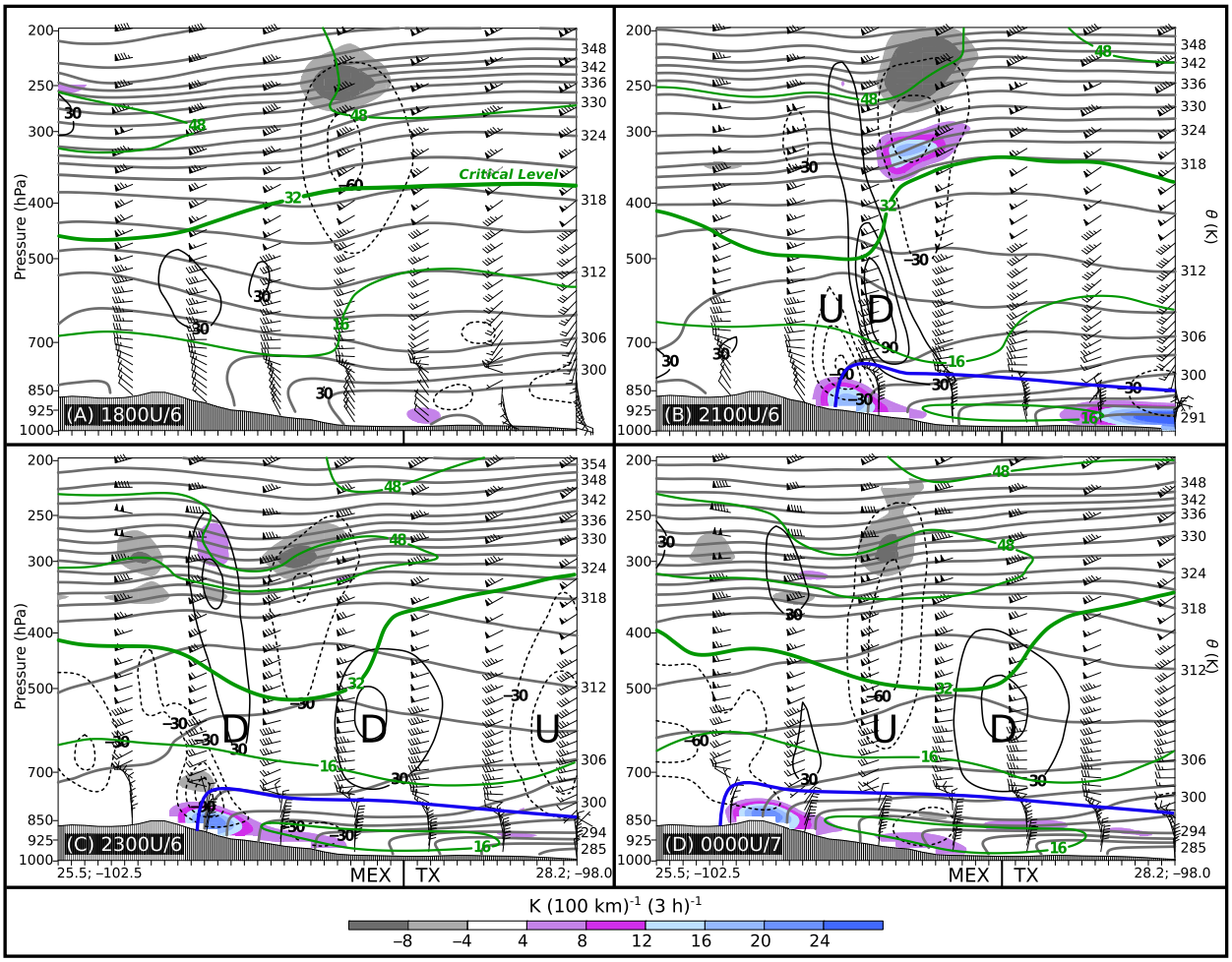

FIG. 17. Vertical cross sections along a transect (shown in Fig. 16) from 25.5°N, 102.5°W to 28.2°N, 98.0°W from the same RUC analyses as Fig. 16 [(a) 1800, (b) 2100, and (c) 2300 UTC 6 Mar, and (d) 0000 UTC 7 Mar]. Shown are wind barbs indicating the horizontal flow (format is as in Fig. 2; direction is not transect relative), isentropes (gray contours; K), isotachs (green contours; m s^{-1}; 32 m s^{-1} contour is thickened and identified as the critical level), ω (black contours; hPa h^{-1}; dashed for negative values), and Petterssen frontogenesis F [shaded according to the color bar; K (100 km)$^{-1}$ (3 h)$^{-1}$]. The blue lines denote the cold front. The Texas–Mexico border is indicated.

accompanied by a rapid decrease then increase in p', a similar pattern in u', increased gustiness, and rainfall shutoff (Figs. 5c,d and 8).

Previous studies show that MH formation within a squall line owes primarily to the lower-tropospheric diabatic cooling due to the evaporation and melting of hydrometeors within the stratiform precipitation region, which leads to an increase in column mass (Fujita 1959; Johnson and Hamilton 1988; Zhang and Gao 1989; Gallus and Johnson 1991; Loehrer and Johnson 1995; Johnson 2001). A WL can subsequently form as the inertia of the sinking motion and low-level divergence, which the diabatic cooling originally generates, causes parcels to descend beyond their level of zero buoyancy and adiabatically warm the column once the cooling locally ceases (e.g., as the stratiform precipitation moves off or dissipates). This overshooting process is favored near the trailing edge of the stratiform region (e.g., Figs. 8–10) where sinking motion, adiabatic warming, and drying can overwhelm the precipitation and shut down the diabatic cooling (Johnson and Hamilton 1988; Johnson et al. 1989; Zhang and Gao 1989; Gallus and Johnson 1991; Stumpf et al. 1991; Loehrer and Johnson 1995; Gallus 1996; Haertel and Johnson 2000; Johnson 2001). It can be inferred that in the presence of a wave duct, wherein low-level N^2 is large, the adiabatic warming and WL response where the diabatic cooling ceases will also be large.

Previous studies have shown that the dynamically induced nonhydrostatic effects of strong downdrafts and density currents within vigorously convecting systems can also be substantial (e.g., Wakimoto 1982; Haertel

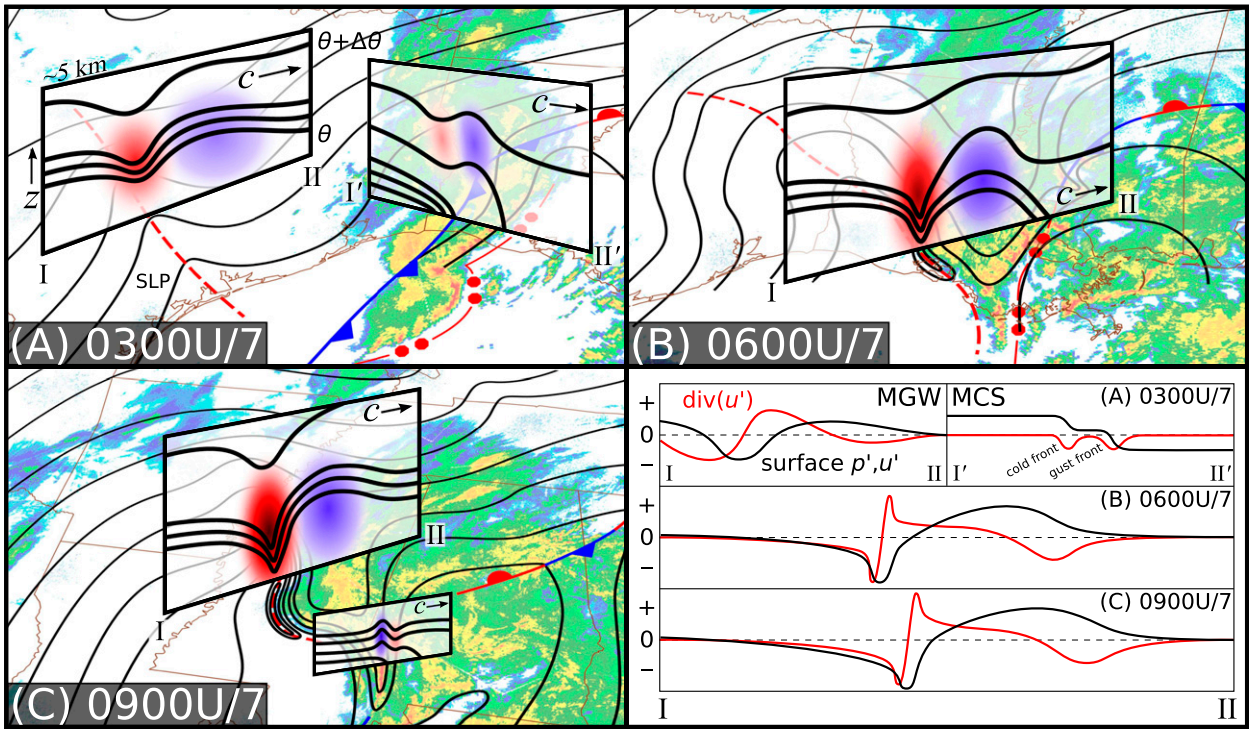

FIG. 18. Schematic depiction of the MGW and its coupling with the rainfall system. (a)–(c) The 3-hourly maps from 0300 to 0900 UTC 7 Mar of mosaic base reflectivity, SLP analyses, and surface fronts from a bird's eye perspective (cf. Figs. 6, 8, and 9); embedded cross sections extend from the surface to ~5 km, which include isentropes (contours; based on Fig. 7) and temperature anomalies associated with adiabatic or moist adiabatic motions (shaded; warm colors indicate positive anomalies; based on Figs. 5, 6, 8, 9, and 11); *c* indicates direction of propagation. (bottom right) Surface p', u', and divergence of u' along the cross sections (for the primary MGW only; based on Fig. 5). Gust front and cold front are indicated.

et al. 2001). The MH–WL couplet, however, is the response to typically weaker vertical motion within the stratiform region (as described just above), which therefore largely obeys hydrostatic balance (Fujita 1959; Johnson and Hamilton 1988; Haertel and Johnson 2000).

Using an idealized hydrostatic model forced by a low-level heat sink representative of the diabatic cooling within a stratiform region, Haertel and Johnson (2000) showed that this MH–WL couplet formation process can be understood as the gravity wave response to the cooling. Correlation between p' and u' in the present case suggests that the MH–WL couplet indeed propagated as a gravity wave (Figs. 5c,d and 8). Therefore, the MGW became synonymous with a MH–WL couplet following its amplification, during and after which time coupling between the MGW and stratiform region was maintained (Figs. 5d–h and 8–10).

The early life of the MGW and its interaction with the MCS is shown schematically in Fig. 18, which invokes information from various observations presented earlier. Around 0300 UTC, the MGW was manifest by modest perturbations in the low-level stable layer, which were connected with adiabatic sinking (rising) motion and warming (cooling) ahead of the surface inverted trough (ridge), as inferred from surface divergence (convergence) in u' (Fig. 18a). The low-level stable layer and weak stratification aloft were conducive to wave ducting (Lindzen and Tung 1976). An intense squall line was situated in a convectively unstable air mass ahead of a cold front, with a trailing stratiform precipitation region extending back over the colder air. Convergence appeared at the cold front and at a gust front leading the convective line.

The low-level stability in the vicinity of the MCS increased by 0600 UTC in connection with low-level diabatic cooling and CAA behind the cold front, which by this time was collocated with the leading squall line (Figs. 8 and 18b). Increased low-level stability made conditions more supportive for gravity wave propagation and wave ducting as the MGW propagated into Louisiana, and also prompted the development of a MH–WL couplet straddling the MCS stratiform region. This small-scale MH–WL couplet projected onto the broader MGW inverted trough–ridge couplet, resulting in focused amplification of the gravity wave signal within and at the trailing edge of the stratiform region.

By 0900 UTC the MGW lost its broad structure away from the stratiform rain shield, retaining only the sharp, intense character of a MH–WL couplet immediately attached to the precipitation (Figs. 9 and 18c). The sharpness of the MGW following this transformation is exemplified by MGW trough passage at GWO, which was characterized by a p' fall of 6.7 hPa in 10 min (embedded within a total fall of 12 hPa), a change in u' of $\sim 17\ \mathrm{m\ s^{-1}}$ over 25 min, and wind gusts of $20\ \mathrm{m\ s^{-1}}$ (Figs. 5f and 9).

The evolution from the broader low-amplitude incipient MGW to a very sharp high-amplitude MGW, which was analogous to a MH–WL couplet in its relationship with precipitation, likely owed to several feedback processes. Enhanced lifting within the low-level convergence region ahead of the MGW ridge was likely important for augmenting precipitation and the release of any convective instability, as suggested by enhanced rainfall banding within the ridge (Figs. 9–11; Uccellini 1975; Stobie et al. 1983). Latent heat release could also serve as an energy supply to the MGW via wave–CISK (Lindzen 1974; Raymond 1984). In a study by Zhang et al. (2001), the coupling between an MGW and elevated convection prompted an increase in the extraction of energy from the background sheared flow at the critical level, which coincided with sudden MGW amplification. Since MGW amplification closely coincided with its coupling with a stratiform rainfall system in the present case, a similar process might have played a role here. Assessing the possible role of these feedbacks requires high-resolution model diagnostics, and is hence left for a future study.

The high-amplitude synoptic flow pattern was also important during the life cycle of the primary MGW (Figs. 2 and 3). It was instrumental in the establishment of strong front-relative, cross-front overriding flow, which spawned a gravity wave atop the frontal stable layer in the fashion of a flow obstacle (Figs. 16 and 17). Synoptic motions also provided a wave duct: a strong frontal stable layer was provided by low-level CAA behind the cold front, and reduced stratification aloft and a mid-tropospheric critical level were provided by strong southwesterly flow aloft (Figs. 2, 3, 7, and 17; Lindzen and Tung 1976).

The coupled MGW–rainfall system was, for a long period, situated beneath a region of notable 300-hPa diffluent ageostrophic flow associated with strong flow curvature and coupled jet streak circulations (Figs. 1 and 2). This upper-level flow pattern was conducive to upper-level divergent outflow, or forcing for ascent, and hence played an important role in the maintenance of the stratiform system. Therefore, since the MGW's maintenance was evidently strongly tied to that of the stratiform system (through the feedbacks described above), this diffluent upper-level flow played an important indirect role in supporting the MGW's persistence. By 1500 UTC, the MGW had rapidly weakened as the upper-level diffluent ageostrophic flow pattern was lost and the stratiform region became disorganized, corroborating that the stratiform rainfall system and upper-level outflow support were both key to the MGW's maintenance (Figs. 2, 4, 12, and 13). Furthermore, the vertical structure of the column was complex during the late stages of the MGW lifetime (Figs. 7e,f). While the exact behavior of MGWs in environments of such complex stratification is unknown, it is possible that the MGW's demise owes partially to a loss of wave ducting.

A narrow wave of elevation ($\mathrm{MGW_{EL}}$) was also observed on 7 March 2008, which was manifest as a sharp inverted ridge along the eastward-moving cold front to the south of the primary MGW (Figs. 1, 9, and 18c). The stark contrast between the primary MGW, a wave of depression, and this $\mathrm{MGW_{EL}}$, was exemplified by contrasting relationships with rainfall. The primary MGW was manifest by a marked suppression of precipitation in association with strong low-level sinking motion and adiabatic warming (e.g., Figs. 5f, 9, and 18c), while the $\mathrm{MGW_{EL}}$ was marked by a pronounced rainband in association with low-level ascending motion and moist adiabatic cooling (Figs. 14a,c and 15a–c). This $\mathrm{MGW_{EL}}$ resembled previously described solitary MGWs formed in response to a density current propagating through a stable air mass (e.g., Christie et al. 1979; Ramamurthy et al. 1993; Koch et al. 2008).

The presence of vigorous deep convection in the warm sector environment immediately east of the frontal boundary and $\mathrm{MGW_{EL}}$ was indicative of much greater convective instability, weaker low-level stability, and hence an unsupportive environment for wave ducting (Figs. 14b and 15d–f). Accordingly, $\mathrm{MGW_{EL}}$ continued on a more northeastward track along the front where wave ducting was supported, and then rapidly dissipated as the front became stationary (Figs. 1, 9, and 10).

7. Summary

This study documents the 7 March 2008 mesoscale gravity wave (MGW) event in which two MGWs caused pronounced local modifications to the sensible weather (Fig. 1). High-frequency surface observations and radar data were used to assess the pressure–wind–precipitation relationships within these MGWs. While propagating within similar environments, the MGWs exhibited stark differences: the primary (i.e., long lived) MGW was manifest by a solitary wave of depression connected with rapid sinking motion, adiabatic warming, and drying,

while the secondary (short lived) MGW was manifest by a wave of elevation (''MGW_{EL}'') associated with rising motion, moist adiabatic cooling, and an embedded narrow rainband. Provided next is a summary of the science findings, unanswered questions, and last, the operational forecasting implications of the study.

The MGW of primary focus in this study exerted strong sensible weather modifications over a large portion of the Southeast United States. It was first observed propagating northeastward across southeastern Texas as a 2–4-hPa inverted trough in surface pressure, with a broader, weaker leading ridge, and a wavelength of ~300 km (Figs. 1, 5a,b, and 6). Genesis of this MGW was tied to the arrival of a cold front at the foot of Mexico's high terrain, which, in the presence of strong cross-front flow, excited a deep gravity wave (Figs. 16b and 17b). This frontal wave then became ducted as cold-air advection behind a cold front provided a low-level stable layer and strongly sheared upper-level flow provided a critical level within a midtropospheric layer of reduced static stability (Figs. 7a and 17c–d).

The MGW later caught up and became coupled with a stratiform precipitation region trailing a squall line, and rapidly amplified as a smaller-scale mesohigh–wake low pressure couplet developed within this stratiform region and within the broader MGW trough–ridge SLP couplet (Figs. 5c,d, 8, and 18). The formation of this mesohigh–wake low couplet only occurred once the environment of the stratiform system became more favorable for wave ducting, indicating the importance of a low-level stable layer for the development of strong surface pressure anomalies through adiabatic warming and cooling.

This MGW amplification led to a slowing of the MGW and decrease in its wavelength (Figs. 1, 8, 9, and 18). The MGW maintained surface pressure falls of $\geq$10 hPa for ~8 h thereafter, with the strongest pressure gradient straddling the sharp back edge of the stratiform rain shield, analogous to a squall-line mesohigh–wake low couplet. The coupling between the MGW and the stratiform precipitation system likely enhanced the ability of the ducted MGW to extract energy from the strongly sheared flow (section 6b), and hence was key to the MGWs maintenance at high amplitude over such a long time period. The dearth of vigorous deep convection during the period of sustained high MGW amplitude reinforces the notion of earlier studies (e.g., Gallus and Johnson 1991) that the stratiform precipitation is of primary importance for maintaining a strong mesohigh–wake low couplet.

A diffluent, highly ageostrophic 300-hPa flow pattern with coupled jet streak circulations was conducive to strong upper-level outflow, hence supporting the maintenance of the stratiform rainfall system. When this upper-level support abated and the stratiform precipitation system became weaker and more disorganized, the MGW rapidly dissipated, indicating the important indirect role of the upper-level flow in the MGW's maintenance.

The MGW_{EL} appeared as a sharp inverted ridge south of the primary MGW within the remnants of a squall line (Figs. 1, 9, 15, and 18). The MGW_{EL} propagated eastward following the motion of a cold front, with a sharp rainband persistently situated within its crest in association with strong low-level rising motion (Figs. 15a–c). MGW_{EL} resembled previously documented waves of elevation connected with density currents advancing through stable air (section 5; e.g., Christie et al. 1979; Ramamurthy et al. 1993; Koch et al. 2008). Rapid dissipation of MGW_{EL} was observed once the front became more stationary, since the adjacent, convectively unstable warm sector environment lacked the necessary wave duct to support it.

Several important questions remain unanswered. What dictated that a solitary wave of depression was generated as a result of the cold front–overriding flow interaction in the present case, versus the wave packet generated in the simulations by Ralph et al. (1999) and Plougonven and Snyder (2007)? What dictated that the primary MGW was a wave of depression, while the short-lived secondary MGW that propagated along the cold front was a wave of elevation? That the environment was presumably similar for these two MGWs suggests that the incipient precipitation system may dictate the subsequent pressure wave response. For instance, the MGW_{EL} evidently formed in response to a predecessor convective rainband, wherein enhanced rising motion was likely responsible for strongly increasing surface pressure as the rainband began to impact an overlying stable layer.

Another open question is whether a squall line mesohigh–wake low couplet would have developed in the absence of the incipient MGW that propagated from southern Texas. It is plausible that ideal conditions for wave ducting, sustained upper-level forcing for ascent, and a preexisting stratiform rain shield were sufficient conditions to produce the extensive mesohigh–wake low couplet that then lasted for nearly 10 h (Fig. 1).

Cases like 7 March 2008 present considerable challenges for the operational forecasting community. The multitude of phenomena that can occur within an environment supporting wave ducting presents considerable uncertainty, as highlighted by the atmosphere's ability to produce MGWs of starkly differing character within similar environments. Gravity wave–related sensible weather effects, such as rapid wind shifts,

strong wind gusts, rapid changes in precipitation intensity, and changes in vertical motion and turbulence character, are of importance to the aviation community and to forecasters responsible for informing the general public.

In the present case, model forecasts missed the frontal deep convection that organized into a bowing squall line, the incipient MGW, and hence the rapid MGW amplification that resulted in large impacts to the sensible weather over a large region (Figs. 3b, 4, and 6). On the other hand, the similar-amplitude MGW event of 2 March 2009 was successfully forecast several days in advance, indicating much higher predictability (A. Seimon 2009, personal communication). Adams-Selin et al. (2013) demonstrated that forecasts of squall lines are highly sensitive to the treatment of microphysics. Therefore, it can be surmised that forecasts of MGW amplification processes related to their coupling with stratiform systems are similarly sensitive. Successful model forecast of MGWs and their interactions with precipitation systems clearly depends on small-scale, highly nonlinear processes. Therefore, uncovering the major MGW forecast sensitivities presents a considerable yet important research challenge.

Acknowledgments. Analysis of the 7 March 2008 MGW event began during a map discussion held at the University at Albany, and all participants, both online and off, are acknowledged. This study substantially benefited from insightful discussions with and comments from Richard Johnson (Colorado State University). We also acknowledge helpful discussions with Steve Saleeby (Colorado State University), Fuqing Zhang (The Pennsylvania State University), and George Bryan (National Center for Atmospheric Research). Comments from two anonymous reviewers, which substantially added to the clarity of this study, are greatly appreciated. Partial research support was provided by University at Albany Collaborative Science, Technology, and Applied Research Program IV Grant NA01NWS4680002 and the University Corporation for Atmospheric Research–NCEP Grant S1071092.

REFERENCES

Adams-Selin, R. D., S. C. van den Heever, and R. H. Johnson, 2013: Impact of graupel parameterization schemes on idealized bow echo simulations. *Mon. Wea. Rev.,* **141,** 1241–1262.

Blumen, W., 1972: Geostrophic adjustment. *Rev. Geophys.,* **10,** 485–528.

Bosart, L. F., and J. P. Cussen Jr., 1973: Gravity wave phenomena accompanying East Coast cyclogenesis. *Mon. Wea. Rev.,* **101,** 446–454.

——, and F. Sanders, 1986: Mesoscale structure in the megalopolitan snowstorm of 11–12 February 1983. Part III: A large-amplitude gravity wave. *J. Atmos. Sci.,* **43,** 924–939.

——, and A. Seimon, 1988: A case study of an unusually intense atmospheric gravity wave. *Mon. Wea. Rev.,* **116,** 1857–1886.

——, W. E. Bracken, and A. Seimon, 1998: A study of cyclone mesoscale structure with emphasis on a large-amplitude inertia-gravity wave. *Mon. Wea. Rev.,* **126,** 1497–1527.

Brunk, I. W., 1949: The pressure pulsation of 11 April 1944. *J. Meteor.,* **6,** 181–187.

Christie, D. R., K. J. Muirhead, and A. L. Hales, 1979: Intrusive density flows in the lower troposphere: A source of atmospheric solitons. *J. Geophys. Res.,* **84** (C8), 4959–4970.

Durran, D. R., and J. B. Klemp, 1982: On the effects of moisture on the Brunt–Väisälä frequency. *J. Atmos. Sci.,* **39,** 2152–2158.

Eom, J. K., 1975: Analysis of the internal gravity wave occurrence of 19 April 1970 in the Midwest. *Mon. Wea. Rev.,* **103,** 217–226.

Ferguson, H. L., 1967: Mathematical and synoptic aspects of a small-scale wave disturbance over the lower Great Lakes area. *J. Appl. Meteor.,* **6,** 523–529.

Ferretti, R., F. Einaudi, and L. W. Uccellini, 1988: Wave disturbances associated with the Red River Valley severe weather outbreak of 10–11 April 1979. *Meteor. Atmos. Phys.,* **39,** 132–168.

Fujita, T. T., 1955: Results of detailed synoptic studies of squall lines. *Tellus,* **7,** 405–436.

——, 1959: Precipitation and cold air production in mesoscale thunderstorm systems. *J. Meteor.,* **16,** 454–466.

Gallus, W. A., 1996: The influence of microphysics in the formation of intense wake lows: A numerical modeling study. *Mon. Wea. Rev.,* **124,** 2267–2281.

——, and R. H. Johnson, 1991: Heat and moisture budgets of an intense midlatitude squall line. *J. Atmos. Sci.,* **48,** 122–146.

Haertel, P. T., and R. H. Johnson, 2000: The linear dynamics of squall line mesohighs and wake lows. *J. Atmos. Sci.,* **57,** 93–107.

——, ——, and S. N. Tulich, 2001: Some simple simulations of thunderstorm outflows. *J. Atmos. Sci.,* **58,** 504–516.

Johnson, R. H., 2001: Surface mesohighs and mesolows. *Bull. Amer. Meteor. Soc.,* **82,** 13–31.

——, and P. J. Hamilton, 1988: The relationship of surface pressure features to the precipitation and airflow structure of an intense midlatitude squall line. *Mon. Wea. Rev.,* **116,** 1444–1473.

——, S. Chen, and J. J. Toth, 1989: Circulations associated with a mature-to-decaying midlatitude mesoscale convective system. Part I: Surface features—heat bursts and mesolow development. *Mon. Wea. Rev.,* **117,** 942–959.

Knippertz, P., J. M. Chagnon, A. Foster, L. Lathouwers, J. H. Marsham, J. Methven, and D. J. Parker, 2010: Research flight observations of a prefrontal gravity wave near the southwestern UK. *Weather,* **65,** 293–297.

Koch, S. E., R. E. Golus, and P. B. Dorian, 1988: A mesoscale gravity wave event observed during CCOPE. Part II: Interactions between mesoscale convective systems and the antecedent waves. *Mon. Wea. Rev.,* **116,** 2545–2569.

——, W. Feltz, F. Fabry, M. Pagowski, B. Geerts, K. M. Bedka, D. O. Miller, and J. W. Wilson, 2008: Turbulent mixing processes in atmospheric bores and solitary waves deduced from profiling systems and numerical simulation. *Mon. Wea. Rev.,* **136,** 1373–1400.

Lalas, D. P., and F. Einaudi, 1976: On the characteristics of gravity waves generated by atmospheric shear layers. *J. Atmos. Sci.,* **33,** 1248–1259.

Lemon, L. R., and C. A. Doswell, 1979: Severe thunderstorm evolution and mesocyclone structure as related to tornadogenesis. *Mon. Wea. Rev.,* **107,** 1184–1197.

Lin, Y.-L., 2010: Mesoscale wave generation and maintenance. *Mesoscale Dynamics,* Cambridge University Press, 64–108.

——, and R. C. Goff, 1988: A study of a mesoscale solitary wave in the atmosphere originating near a region of deep convection. *J. Atmos. Sci.,* **45,** 194–206.

Lin, Y., and F. Zhang, 2008: Tracking gravity waves in baroclinic jet-front systems. *J. Atmos. Sci.,* **65,** 2402–2415.

Lindzen, R. S., 1974: Wave-CISK in the tropics. *J. Atmos. Sci.,* **31,** 156–179.

——, and K.-K. Tung, 1976: Banded convective activity and ducted gravity waves. *Mon. Wea. Rev.,* **104,** 1602–1617.

Loehrer, S. M., and R. H. Johnson, 1995: Surface pressure and precipitation life cycle characteristics of PRE-STORM mesoscale convective systems. *Mon. Wea. Rev.,* **123,** 600–621.

Miller, D. A., and F. Sanders, 1980: Mesoscale conditions for the severe convection of 3 April 1974 in the east-central United States. *J. Atmos. Sci.,* **37,** 1041–1055.

Nadolski, V. L., 1998: Automated Surface Observing System (ASOS) user's guide. NOAA, Department of Defense, Federal Aviation Administration, U. S. Navy, 74 pp. [Available online at http://www.nws.noaa.gov/asos/pdfs/aum-toc.pdf.]

Neiman, P. J., F. M. Ralph, R. L. Weber, T. Uttal, L. B. Nance, and D. H. Levinson, 2001: Observations of nonclassical frontal propagation and frontally forced gravity waves adjacent to steep topography. *Mon. Wea. Rev.,* **129,** 2633–2659.

Parker, M. D., and R. H. Johnson, 2000: Organizational modes of midlatitude mesoscale convective systems. *Mon. Wea. Rev.,* **128,** 3413–3436.

Pecnick, M. J., and J. A. Young, 1984: Mechanics of a strong subsynoptic gravity wave deduced from satellite and surface observations. *J. Atmos. Sci.,* **41,** 1850–1862.

Petterssen, S., 1936: Contribution to the theory of frontogenesis. *Geofys. Publ.,* **11** (6), 1–27.

——, 1956: *Motion and Motion Systems.* Vol. 2, *Weather Analysis and Forecasting,* McGraw-Hill, 428 pp.

Plougonven, R., and C. Snyder, 2007: Inertia–gravity waves spontaneously generated by jets and fronts. Part I: Different baroclinic life cycles. *J. Atmos. Sci.,* **64,** 2502–2520.

——, and F. Zhang, 2014: Internal gravity waves from atmospheric jets and fronts. *Rev. Geophys.,* doi:10.1002/2012RG000419, in press.

Ralph, F. M., M. Crochet, and S. V. Venkateswaran, 1993: Observations of a mesoscale ducted gravity wave. *J. Atmos. Sci.,* **50,** 3277–3291.

——, P. J. Neiman, and T. L. Keller, 1999: Deep-tropospheric gravity waves created by leeside cold fronts. *J. Atmos. Sci.,* **56,** 2986–3009.

Ramamurthy, M. K., R. M. Rauber, B. P. Collins, and N. K. Malhotra, 1993: A comparative study of large-amplitude gravity-wave events. *Mon. Wea. Rev.,* **121,** 2951–2974.

Raymond, D. J., 1984: A wave-CISK model of squall lines. *J. Atmos. Sci.,* **41,** 1946–1958.

Snyder, C., W. C. Skamarock, and R. Rotunno, 1993: Frontal dynamics near and following frontal collapse. *J. Atmos. Sci.,* **50,** 3194–3212.

——, D. J. Muraki, R. Plougonven, and F. Zhang, 2007: Inertia–gravity waves generated within a dipole vortex. *J. Atmos. Sci.,* **64,** 4417–4431.

——, R. Plougonven, and D. J. Muraki, 2009: Mechanisms for spontaneous gravity wave generation within a dipole vortex. *J. Atmos. Sci.,* **66,** 3464–3478.

Stobie, J. G., F. Einaudi, and L. W. Uccellini, 1983: A case study of gravity waves–convective storms interaction: 9 May 1979. *J. Atmos. Sci.,* **40,** 2804–2830.

Stumpf, G. J., R. H. Johnson, and B. F. Smull, 1991: The wake low in a midlatitude mesoscale convective system having complex convective organization. *Mon. Wea. Rev.,* **119,** 134–158.

Tepper, M., 1951: On the desiccation of a cloud bank by a propagated pressure wave. *Mon. Wea. Rev.,* **79,** 61–70.

Trexler, C. M., and S. E. Koch, 2000: The life cycle of a mesoscale gravity wave as observed by a network of Doppler wind profilers. *Mon. Wea. Rev.,* **128,** 2423–2446.

Uccellini, L. W., 1975: A case study of apparent gravity wave initiation of severe convective storms. *Mon. Wea. Rev.,* **103,** 497–513.

——, and S. E. Koch, 1987: The synoptic setting and possible energy sources for mesoscale wave disturbances. *Mon. Wea. Rev.,* **115,** 721–729.

Van Tuyl, A. H., and J. A. Young, 1982: Numerical simulation of nonlinear jet streak adjustment. *Mon. Wea. Rev.,* **110,** 2038–2054.

Wagner, A. J., 1962: Gravity wave over New England, April 12, 1961. *Mon. Wea. Rev.,* **90,** 431–436.

Wakimoto, R. M., 1982: Life cycle of thunderstorm gust fronts as viewed with Doppler radar and rawinsonde data. *Mon. Wea. Rev.,* **110,** 1060–1082.

Wang, S., and F. Zhang, 2010: Source of gravity waves within a vortex-dipole jet revealed by a linear model. *J. Atmos. Sci.,* **67,** 1438–1455.

——, ——, and C. Snyder, 2009: Generation and propagation of inertia–gravity waves from vortex dipoles and jets. *J. Atmos. Sci.,* **66,** 1294–1314.

Zhang, D.-L., and K. Gao, 1989: Numerical simulation of an intense squall line during 10–11 June 1985 PRE-STORM. Part II: Rear inflow, surface pressure perturbations, and stratiform precipitation. *Mon. Wea. Rev.,* **117,** 2067–2094.

Zhang, F., 2004: Generation of mesoscale gravity waves in upper-tropospheric jet–front systems. *J. Atmos. Sci.,* **61,** 440–457.

——, and S. E. Koch, 2000: Numerical simulations of a gravity wave event over CCOPE. Part II: Waves generated by an orographic density current. *Mon. Wea. Rev.,* **128,** 2777–2796.

——, ——, C. A. Davis, and M. L. Kaplan, 2001: Wavelet analysis and the governing dynamics of a large-amplitude mesoscale gravity-wave event along the East Coast of the United States. *Quart. J. Roy. Meteor. Soc.,* **127,** 2209–2245.